

Structure of an open K_{ATP} channel reveals tandem PIP_2 binding sites mediating the Kir6.2 and SUR1 regulatory interface

Received: 18 January 2024

Accepted: 8 March 2024

Published online: 20 March 2024

 Check for updatesCamden M. Driggers¹✉, Yi-Ying Kuo¹, Phillip Zhu¹, Assmaa ElSheikh^{1,2} & Show-Ling Shyng¹✉

ATP-sensitive potassium (K_{ATP}) channels, composed of four pore-lining Kir6.2 subunits and four regulatory sulfonylurea receptor 1 (SUR1) subunits, control insulin secretion in pancreatic β -cells. K_{ATP} channel opening is stimulated by PIP_2 and inhibited by ATP. Mutations that increase channel opening by PIP_2 reduce ATP inhibition and cause neonatal diabetes. Although considerable evidence has implicated a role for PIP_2 in K_{ATP} channel function, previously solved open-channel structures have lacked bound PIP_2 , and mechanisms by which PIP_2 regulates K_{ATP} channels remain unresolved. Here, we report the cryoEM structure of a K_{ATP} channel harboring the neonatal diabetes mutation Kir6.2-Q52R, in the open conformation, bound to amphipathic molecules consistent with natural C18:0/C20:4 long-chain PI(4,5)P₂ at two adjacent binding sites between SUR1 and Kir6.2. The canonical PIP_2 binding site is conserved among PIP_2 -gated Kir channels. The non-canonical PIP_2 binding site forms at the interface of Kir6.2 and SUR1. Functional studies demonstrate both binding sites determine channel activity. Kir6.2 pore opening is associated with a twist of the Kir6.2 cytoplasmic domain and a rotation of the N-terminal transmembrane domain of SUR1, which widens the inhibitory ATP binding pocket to disfavor ATP binding. The open conformation is particularly stabilized by the Kir6.2-Q52R residue through cation- π bonding with SUR1-W51. Together, these results uncover the cooperation between SUR1 and Kir6.2 in PIP_2 binding and gating, explain the antagonistic regulation of K_{ATP} channels by PIP_2 and ATP, and provide a putative mechanism by which Kir6.2-Q52R stabilizes an open channel to cause neonatal diabetes.

The K_{ATP} channel expressed in pancreatic islet β -cells is a principal homeostatic regulator of insulin secretion^{1–3}. Composed of four pore-forming Kir6.2 subunits and four regulatory sulfonylurea receptor 1 (SUR1) subunits^{4,5}, K_{ATP} channels influence the resting membrane potential, thus action potential firing, Ca^{2+} entry, and insulin secretion. The activity of K_{ATP} channels is dynamically regulated by glucose changes via intracellular ATP and MgADP, which bind to inhibitory and

stimulatory sites to close and open the channel, respectively^{6,7}. This enables insulin secretion to follow fluctuations in glucose concentrations. The central role of K_{ATP} channels in insulin secretion and glucose homeostasis is underscored by dysregulated insulin secretion and blood glucose in humans bearing K_{ATP} mutations: loss-of-function mutations cause congenital hyperinsulinism characterized by persistent insulin secretion despite life-threatening hypoglycemia^{8,9};

¹Department of Chemical Physiology and Biochemistry, School of Medicine, Oregon Health & Science University, Portland, OR 97239, USA. ²Department of Medical Biochemistry, Tanta University, Tanta, Egypt. ✉e-mail: driggerc@ohsu.edu; shyngs@ohsu.edu

conversely, gain-of-function channel mutations result in neonatal diabetes due to insufficient insulin secretion¹⁰.

In addition to adenine nucleotides-dependent regulation, membrane phosphoinositides participate in the gating activation of K_{ATP} channels^{11,12}, as they do all other eukaryotic Kir channels¹³. PI(4,5)P₂ (denoted as PIP₂ unless specified) is the most abundant phosphoinositide in the plasma membrane¹⁴, with PIP₂ containing arachidonoyl (C20:4) and stearoyl (C18:0) acyl chains being the most dominant species in mammalian cells¹⁵. In inside-out patch-clamp recordings, application of C18:0/C20:4 long-chain PIP₂ to the cytoplasmic side of the membrane patch resulted in stable increases in K_{ATP} channel open probability (P_o) and a gradual decrease in channel sensitivity to ATP inhibition; whereas scavenging membrane PIP₂ with poly-lysine decreases channel P_o ^{11,12}. Because increasing channel P_o by PIP₂ also decreases channel sensitivity to ATP inhibition^{11,12}, a joint regulatory mechanism involving allosteric or binding competition between the two ligands has seemed likely¹⁶. In particular, the effect of PIP₂ on K_{ATP} channels has been assumed to derive from a putative conserved binding site in Kir6.2 having a position homologous to the PIP₂ binding site previously identified in crystal and cryoEM structures of Kir2 and Kir3^{17–20}. Unlike other Kir channels however, gating of Kir6.2 by PIP₂ is strongly modulated by its regulatory subunit SUR1. Compared to the fully assembled K_{ATP} channels, Kir6.2 channels lacking SUR1 partners display more than 10-fold lower P_o ^{11,16,21}, which reflects reduced PIP₂ binding or gating, and are less sensitive to PIP₂ stimulation^{11,16}. Of particular interest, the SUR1 N-terminal transmembrane domain, TMD0, which interfaces with Kir6.2^{22–24}, is sufficient to confer the high P_o of wild-type (WT) channels^{25,26}, implicating a crucial role of SUR1-TMD0 in controlling Kir6.2 response to PIP₂.

To date, cryoEM structures of K_{ATP} channels determined for a variety of liganded and mutational states have yielded a structural spectrum encompassing open, closed, and inactivated conformations (reviewed in^{6,7,27}). Careful comparisons have suggested mechanisms by which channel activity is regulated by the SUR subunit and nucleotides. However, confusion has grown regarding PIP₂ binding and gating. Two recently reported open- and pre-open mutant K_{ATP} channel cryoEM structures lack discernible PIP₂ at the putative binding site^{28,29}, even when excess synthetic short-chain diC8-PI(4,5)P₂ was added to the sample in the case of the pre-open structure³⁰. Furthermore, purified WT K_{ATP} channels reconstituted in lipid bilayers lacking PIP₂ showed single channel openings²⁸. These reports suggest that PIP₂ binding may be inessential for open channel transition²⁸. Thus, notwithstanding robust data indicating PIP₂ involvement in physiological channel activation^{11,31,32}, how PIP₂ binds and modulates K_{ATP} channels remains enigmatic.

Our approach to understanding K_{ATP} channel activation and PIP₂ binding involved determining channel structure bound to PIP₂ by (1) incubating membranes expressing K_{ATP} channels with long-chain PIP₂ known to stably activate the channel^{11,12,33}, and (2) employing a Kir6.2 variant containing the neonatal diabetes-causing mutation Q52R (denoted Kir6.2^{Q52R})^{34,35}. Kir6.2^{Q52R} markedly increases channel P_o and causes a 20-fold decrease in channel sensitivity to ATP inhibition^{34,35}. Higher P_o could result from enhanced PIP₂ binding or its effect on gating. Intriguingly, the effect of this mutation on channel gating is SUR1-dependent. When Kir6.2 was manipulated to express at the cell surface without co-assembly with SUR1 (by deleting the Arg-Lys-Arg endoplasmic reticulum retention signal at the C-terminal region of Kir6.2), introducing the Q52R mutation had little effect on the P_o and ATP sensitivity³⁶. The SUR1-dependent overactivity imparted by the Kir6.2-Q52R mutation indicated the possibility to probe the regulatory interaction between SUR1 and membrane PIP₂ on Kir6.2 gating.

Here, we present the cryoEM structure of the K_{ATP} channel harboring the neonatal diabetes Q52R mutation (hereinafter referred to as the SUR1/Kir6.2^{Q52R} channel) in an open conformation bound to amphipathic molecules consistent with natural C18:0/C20:4 long-

chain PI(4,5)P₂. Surprisingly, our structural model suggests that two PIP₂ molecules bind in tandem in the open channel at the interface between Kir6.2 and SUR1. At each Kir6.2-SUR1 interface, one PIP₂ molecule is bound within the site that is conserved among Kir channels (referred to as the canonical site), and a second PIP₂ molecule is at an adjacent site, stacked within the regulatory interface between Kir6.2 and SUR1-TMD0 (referred to as the non-canonical site). The open channel conformation is further stabilized by direct interaction between Q52R of Kir6.2 and W51 located in TMD0 of SUR1. Accounting for decades of evidence from functional perturbation studies, the PIP₂-bound SUR1/Kir6.2^{Q52R} K_{ATP} structure unveils the agonist binding of PIP₂ in K_{ATP} channels, revealing that in addition to the ancestral Kir PIP₂ site, the incorporation of the regulatory SUR1 subunit creates a second regulatory PIP₂ binding site. The results uncover a mechanism through which SUR1, by cooperating with Kir6.2 for PIP₂ binding, stabilizes the K_{ATP} channel in an open state to control activity, and illuminate a putative molecular mechanism by which a neonatal diabetes-associated Kir6.2 mutation causes overactive K_{ATP} channels.

Results

Structure of an open SUR1/Kir6.2^{Q52R} K_{ATP} channel bound to PIP₂

To purify the neonatal diabetes variant SUR1/Kir6.2^{Q52R} K_{ATP} channel, we co-expressed Kir6.2^{Q52R} and SUR1 as independent polypeptides by transducing adherent mammalian COSm6 cells with recombinant adenovirus packaged with genes for rat Kir6.2^{Q52R} and FLAG-tagged hamster SUR1 (see Methods). Prior functional experiments have shown that the activating effects of long-chain PIP₂ are long-lasting and resistant to subsequent washout, indicating stable partition into the membrane^{11,12,33}. By contrast, the effects of synthetic short-chain PIP₂ such as diC8-PIP₂ are highly reversible^{33,37}. Accordingly, we prepared a membrane fraction of COSm6 cells expressing the mutant channel, and enriched the native membranes with brain PIP₂, primarily containing C18:0/C20:4 long-chain PI(4,5)P₂ (Avanti Polar Lipids), before detergent solubilization. We anticipated that the addition of long-chain PIP₂ prior to detergent extraction would stably incorporate PIP₂ resistant to washout in subsequent purification steps to facilitate the capture of PIP₂-bound channel structure. K_{ATP} channels were purified via the N-terminal FLAG-tag on SUR1 and spotted on graphene oxide (GO)-coated grids for cryoEM (see Methods). To maximize channels in PIP₂-bound open conformations, no ATP or ADP were added to the sample.

CryoEM micrographs showed mostly full SUR1/Kir6.2^{Q52R} K_{ATP} channel particles (Supplementary Fig. 1a). 2D classes indicate an ordered Kir6.2 and SUR1-TMD0, with a relatively more blurred SUR1-ABC core especially the nucleotide-binding domains (NBDs) (Supplementary Fig. 1a–d). A non-uniform refinement with C4 symmetry using all good particles from 2D classification (70,638) in cryoSPARC resulted in an un-masked reconstruction of the full channel at 3.9 Å using the gold-standard Fourier shell correlation (GSFSC) cutoff of 0.143 (see Methods). The electron potential map shows a relatively weak signal for TMD2 and NBD2 of SUR1 (Supplementary Fig. 1), indicating higher mobility of these domains. Multiple rounds of ab initio reconstruction without symmetry imposed (Supplementary Fig. 1a) yielded a best 3D class containing 14,115 particles, which following a C4 non-uniform refinement in cryoSPARC with auto-masking that excluded SUR1-NBD2 resulted in a final map reconstruction of 2.9 Å by GSFSC within the autoFSC mask (Fig. 1a, Supplementary Fig. 1a–d), or 3.3 Å resolution by GSFSC within a mask that includes the full K_{ATP} channel. Since the full channel map derived from the C4 non-uniform refinement has the best overall resolution, showing a highly ordered Kir6.2 tetramer core and SUR1-TMD0 with local resolutions < 2.9 Å, the map was used for model building (Fig. 1, Supplementary Fig. 1, Supplementary Table 1). The cryoEM map reconstruction revealed amphipathic densities that are fit by two bound PIP₂ molecules at the regulatory interface of Kir6.2 and SUR1, an open Kir6.2 pore, and molecular rearrangements at the SUR1-

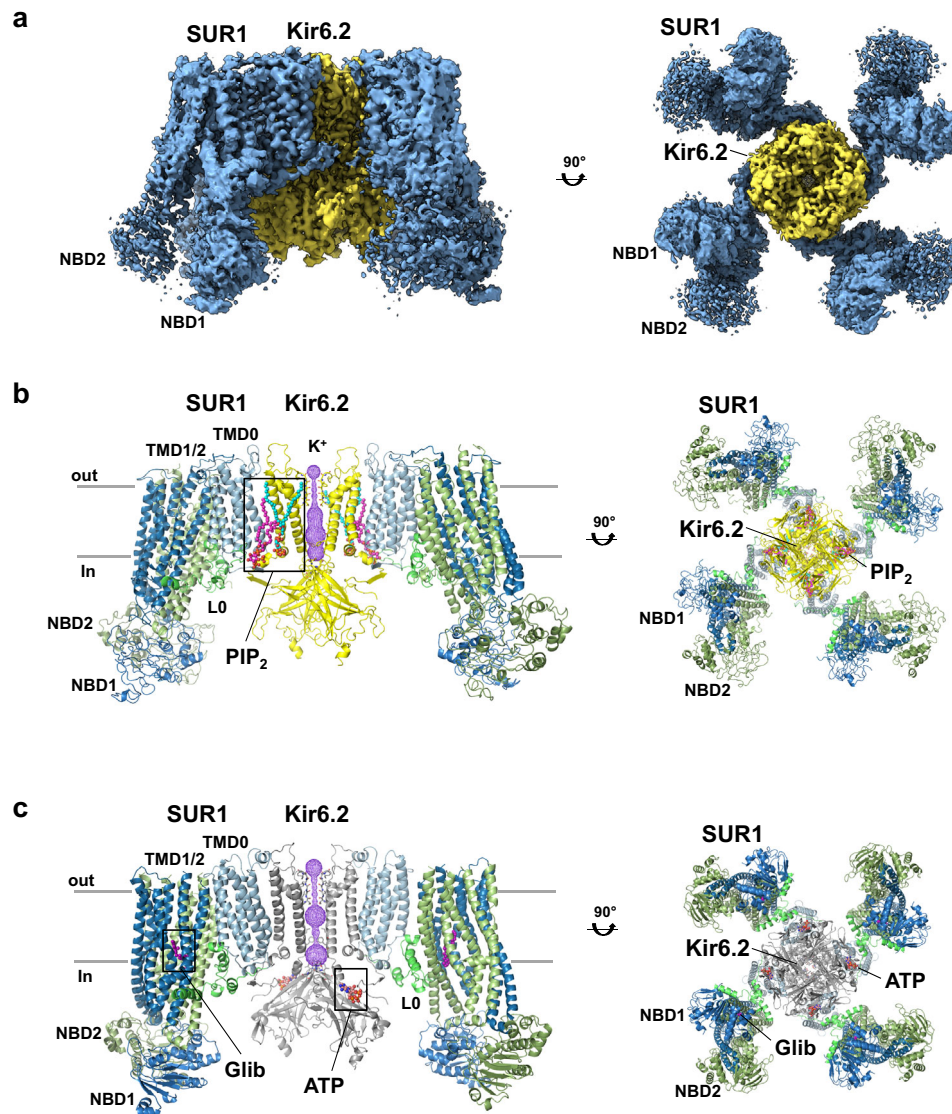


Fig. 1 | CryoEM structure of PIP₂-bound, open SUR1/Kir6.2^{Q52R} K_{ATP} channel.
a The 2.9 Å cryoEM map (the micelle not shown), from C4 non-uniform refinement of 14,115 particles, shown from the side and bottom (cytoplasmic view). **b** Structural model of the SUR1/Kir6.2^{Q52R} K_{ATP} channel in complex with PIP₂. The potassium ion selectivity filter is shown as sticks with oxygens colored red, the K⁺ conduction pathway is shown as purple mesh. Only two Kir6.2 and two SUR1 subunits are shown

in the side view for clarity. A view rotated 90° (cytoplasmic view) displays all four Kir6.2 subunits and all four SUR1 subunits. **c** Structural model of a closed WT SUR1/Kir6.2 K_{ATP} channel in complex with ATP and glibenclamide (Glib) (PDB ID 6BAA), shown for comparison and rendered in PyMOL similar to **(b)**, except for the Kir6.2 subunits which are colored gray.

Kir6.2 interface critical to gating, as we describe in detail in the following sections.

Additional analysis of all particles from the 2D classes employed a strategy of symmetry expansion and focused 3D classification (using a mask of Kir6.2^{Q52R} tetramer plus one SUR1 subunit to circumvent the flexibility of the SUR1 subunits), revealing a spectrum of conformational classes with distinct Kir6.2-cytoplasmic domain (CTD) and SUR1 positions (Supplementary Fig. 2). The two most extreme conformations include a dominant conformation at -3.3 Å (no C4 symmetry imposed) that is nearly identical to the map derived from the C4 non-uniform refinement described above, and a minor conformation at 6.9 Å (Supplementary Fig. 2a). Superimposition of the two extreme conformations revealed differences in the K⁺ pore path, rotation of the Kir6.2^{Q52R}-CTD, and distance of the Kir6.2^{Q52R}-CTD to the membrane (Supplementary Fig. 2b–d), as well as the absence or presence of the cryoEM density corresponding to the N-terminal domain of Kir6.2^{Q52R} (the distal 30 amino acids, referred to as KNtp; Supplementary Fig. 2e).

Relative to the high resolution dominant class, the low resolution minor class shows a constricted Kir6.2^{Q52R} pore, a clockwise-rotated (viewed from the cytoplasmic side) Kir6.2^{Q52R}-CTD that is moved away from the membrane and into the cytoplasm, and a clear KNtp density in the central cleft of the SUR1-ABC core. Moreover, the SUR1-ABC core is rotated towards the Kir6.2^{Q52R} tetramer and moved downward from the outer membrane (Supplementary Fig. 2c, d). These features highly resemble our previously published closed apo (no PIP₂, nucleotides, or pharmacological inhibitors added) WT K_{ATP} channel structure (PDB ID 7UQR)³⁸, and indicate the minor conformation isolated from our sample represents an apo closed SUR1/Kir6.2^{Q52R} structure (and will be referred to as such hereinafter) even with the exogenously added long-chain PIP₂.

Tandem PIP₂ binding at the interface of Kir6.2 and SUR1

The cryoEM map of the PIP₂-bound SUR1/Kir6.2^{Q52R} K_{ATP} channel showed densities of two amphipathic molecules, occupying sites in a

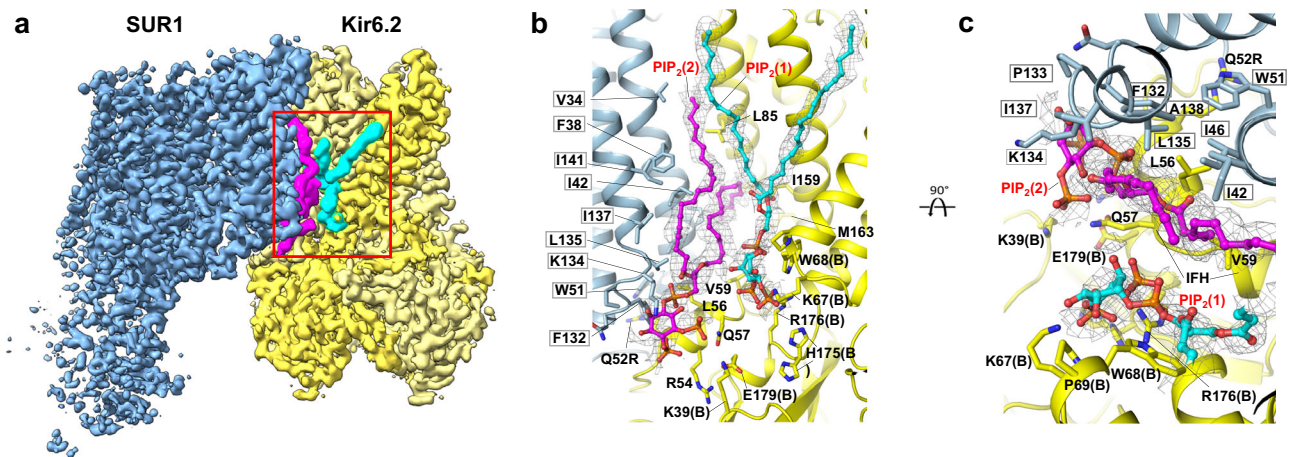


Fig. 2 | Two PIP₂ binding sites at the interface of Kir6.2 and SUR1. **a** CryoEM map features of two PIP₂ molecules colored in cyan and magenta (0.08 V, 4.0 σ contour), respectively. **b** Structural model of the PIP₂ binding pocket (red boxed region in **a**) viewed from the side, with cryoEM density of PIP₂ shown as gray mesh. Residues

from both Kir6.2 (adjacent subunit denoted “B”) and SUR1 (gray outline) surrounding bound PIP₂ molecules are labeled. **c** Structural model of the PIP₂ binding pocket view from the top (extracellular side).

large pocket at the Kir6.2-SUR1 interface near the inner leaflet of the membrane bilayer (Fig. 2a). The first amphipathic molecule sits in the predicted canonical PIP₂ binding site of Kir6.2 based on comparisons with the homologous structures of Kir channels Kir2 and Kir3/GIRK bound to PIP₂^{17–20} (colored cyan in all relevant figures). The second amphipathic molecule, which has stronger map features (colored magenta in relevant figures) than the one in the canonical PIP₂ binding site, is nestled between SUR1 and the canonical PIP₂ binding site and in contact with both Kir6.2 and SUR1 subunits (Fig. 2). We modeled these densities as two C18:0/C20:4 PI(4,5)P₂ molecules (Figs. 1b, 2b and c, and Supplementary Fig. 3a and b) based on the following. First, C18:0/C20:4 PI(4,5)P₂ is the dominant species in the brain PIP₂ present in our sample (~75%)¹⁵, and both amphipathic molecule densities have map features for the phospho-head groups as well as long acyl chains consistent with C18:0/C20:4 PI(4,5)P₂ (monomer ID PT5) (Fig. 2b, c, and Supplementary Fig. 3b). Second, the amphipathic molecule densities are less well fit by other common endogenous phospholipids such as phosphatidylethanolamine (PE) or phosphatidylserine (PS) with smaller head groups (Supplementary Fig. 3c, d), or digitonin (Supplementary Fig. 3e), the detergent used to solubilize the membrane. Third, comparison with other open cryoEM K_{ATP} channel structures solved in the absence of long-chain PIP₂, including the open SUR1/Kir6.2^{C166S, G334D} channel structure and the pre-open SUR1-Kir6.2^{H175K} fusion channel structure, reveals clear differences in the non-protein cryoEM densities in this pocket (Supplementary Fig. 4a, b). However, other residual endogenous lipids or lipid species other than C18:0/C20:4 PI(4,5)P₂ in the brain PIP₂ used for the experiment may also contribute to the observed densities. In addition to lipid densities at the SUR1-Kir6.2 interface, three other well-resolved lipid map features at the inner leaflet of the membrane bilayer were bound between SUR1-TMDO and SUR1-TMD1. These were best modeled by the common phospholipids phosphatidylethanolamine and phosphatidylserine (Supplementary Fig. 3f, g). Of note, lipid or detergent densities were also observed in the outer leaflet space (Supplementary Fig. 3a); however, they were not sufficiently resolved to warrant modeling.

Structural analysis surrounding the PIP₂ head groups. The head group of PIP₂ at the canonical site forms extensive polar interactions with surrounding residues (Fig. 2b, c). The phosphate groups are coordinated directly by Kir6.2 residues R176 and K67 while Kir6.2-W68 forms close interaction with the inositol ring, although K170, which is about 4.5 Å away and H175, which is about 5.5 Å away, are also in close

proximity. Most of the head group-interacting residues are conserved in Kir2 and Kir3 channels with the exception of Kir6.2-P69 and H175, which in Kir2 and Kir3 are an arginine and a lysine, respectively, and shown to coordinate PIP₂ binding in Kir2 and Kir3^{17–20}. The amino acid difference at these two positions would weaken Kir6.2-PIP₂ interactions, which may explain the lower phosphoinositide head group specificity compared to other Kir channels³³. Interestingly, Kir6.2-H175 sidechain exhibited two rotameric positions in the PIP₂-bound SUR1/Kir6.2^{Q52R} channel cryoEM density map: one oriented towards PIP₂ in the conserved binding site and the other towards E179 in the same Kir6.2 subunit (Fig. 2b). Kir6.2-H175 has been previously implicated in acid-induced activation of K_{ATP} channels between pH 7.4 and 6.8 with a pK of 7.16³⁹. Mutating Kir6.2-H175 to lysine, which mimics protonated state of H175, increased basal channel activity and abolished channel activation by pH, suggesting protonation of H175 favors channel opening³⁹. Moreover, mutating Kir6.2-E179 to Q greatly attenuated pH-induced channel activation, suggesting Kir6.2-E179 also has a role in acid activation of K_{ATP} channels. Our structural observation that H175 sidechain has interaction with PIP₂ head group in the canonical site and with Kir6.2-E179 is consistent with the aforementioned mutation-function correlation studies. Since our protein sample was prepared at pH-7.5 (see Methods), which predicts H175 to be largely unprotonated based on the pK of acid activation of the channel of 7.16, it remains to be determined how protonation of H175 at lower pH that activates the channel alters interaction with PIP₂ and E179 to stabilize channel opening.

The PIP₂ molecule in the non-canonical site is coordinated by both Kir6.2 and SUR1 subunits (Figs. 1b and 2). Here, the PIP₂ head group interacts with surrounding residues including K39 and Q57 of Kir6.2, and N131, F132, P133, and K134 of SUR1. Previously we have noted that in closed K_{ATP} structures, SUR1-K134, located in intracellular loop (ICL) 2 of SUR1-TMDO, has its sidechain directed towards cryoEM densities in the predicted PIP₂ binding pocket tentatively modeled as phosphatidylserines³⁸. Based on the observation, we mutated SUR1-K134 to alanine and found it reduced channel *P_o*, which was recovered by adding exogenous PIP₂³⁸. Our PIP₂-bound SUR1/Kir6.2^{Q52R} open structure now shows that SUR1-K134 is involved in PIP₂ binding but at the non-canonical site, directly explaining the mutational study result.

Structural interactions with the acyl chains of PIP₂. Most phospholipids present a range of molecular species comprising acyl chains of diverse length and saturation. However, mammalian PIPs show the predominance of a single hydrophobic backbone composed of

arachidonoyl (C20:4) and stearoyl (C18:0) chains¹⁵. In the PIP₂-bound SUR1/Kir6.2^{Q52R} open K_{ATP} channel structure determined with an enrichment of natural brain PIP₂ in the membrane, we observed cryoEM densities consistent with branched long acyl chains for both PIP₂ molecules and modeled them as such to best fit the densities (Fig. 2b and Supplementary Fig. 3b). The PIP₂ bound at the canonical site mediates interactions between Kir6.2 subunits. While one chain is primarily associated with the outer TM helix of the Kir6.2 subunit that coordinates head group binding (modeled as the arachidonoyl chain), the other chain sits between the TM helices of the adjacent Kir6.2 subunit (modeled as the stearoyl chain; Fig. 2b). CryoEM density at this canonical PIP₂ binding pocket was previously reported by our group and others, but in those studies the map features lack lipid acyl tails and could not be ascertained as PIP₂^{30,38,40,41} (Supplementary Fig. 4a, b). The lipid tails of the PIP₂ molecule in the non-canonical site are sandwiched between SUR1-TMD0 and Kir6.2-TMs, with one chain running along TM1 and TM4 of SUR1-TMD0 (modeled as the arachidonoyl chain) and the other between TM1 of SUR1-TMD0 and TMs of Kir6.2 (modeled as the stearoyl chain), and have non-polar interactions with SUR1 (V34, F38, I42, P45, I46, L135, I137, A138, I141) and Kir6.2 (L56, V59, I59) respectively (Fig. 2b, c). Long-chain PIP₂ stably activates K_{ATP} channels^{11,12}; in contrast, activation of channels by synthetic short-chain PIP₂ such as diC8-PIP₂ is readily reversible³³. The extensive hydrophobic interactions between channel subunits and the long acyl chains of C18:0/C20:4 PI(4,5)P₂ observed in our structure may contribute to the apparent increase in stability of channel activation by long-chain PIP₂.

Functional role of the two PIP₂ binding sites. To probe the functional role of the two PIP₂ binding sites, we compared the PIP₂ response of WT channels to channels containing the following mutations: Kir6.2^{R176A}, which is predicted to weaken the canonical PIP₂ binding site; SUR1^{K134A}, which is expected to weaken the non-canonical PIP₂ binding site; Kir6.2^{R176A} and SUR1^{K134A}, which weaken both PIP₂ binding sites (Fig. 3a). Exposure to brain-derived C18:0/C20:4 PI(4,5)P₂ increased activity that is resistant to washout and decreased ATP inhibition over time in WT channels, as has been shown previously^{11,12}. Similar effects of PIP₂ were observed in all three mutant channels (Fig. 3a). However, the initial currents upon membrane excision, the extent of current increase upon PIP₂ stimulation, and the PIP₂ exposure time required for currents to reach maximum showed striking differences among the different channels (Fig. 3b–d). WT channels exhibited robust activity upon membrane excision into ATP-free solution, and currents increased by 1.48 ± 0.23 -fold (Fig. 3a) that plateaued within 1 min of PIP₂ exposure. Perturbation of the non-canonical PIP₂ binding site by SUR1^{K134A} resulted in channels that showed reduced initial currents (596.91 ± 218.23 pA vs. 1488.53 ± 348.86 pA of WT channels), which increased by 3.96 ± 0.47 -fold in response to PIP₂. Perturbation of the canonical PIP₂ binding site by Kir6.2^{R176A} markedly reduced initial currents (42.44 ± 11.12 pA), which increased by 48.74 ± 18.25 -fold after PIP₂ exposure. Combining SUR1^{K134A} and Kir6.2^{R176A} yielded channels that showed barely detectable currents at patch excision (12.62 ± 4.34 pA) and a dramatic 299.65 ± 121.72 -fold current increase by PIP₂. All three mutants also required longer PIP₂ exposure to reach maximum currents in the order of double mutant (419.33 ± 57.86 sec) > Kir6.2^{R176A} (298.57 ± 73.76 s) > SUR1^{K134A} (193.83 ± 33.66 s), compared to WT channels (33.17 ± 3.18 sec) (Fig. 3d). These results demonstrate that both PIP₂ binding sites have functional roles in K_{ATP} channel activity.

Kir6.2 pore in open conformation

In Kir channels, there are three constriction points in the K⁺ conduction pathway: the selectivity filter on the extracellular side, the inner helix gate at the helix bundle crossing where four inner helices (M2) converge, and the G-loop gate in the cytoplasmic pore just below the

membrane¹³. The structure of the PIP₂-bound SUR1/Kir6.2^{Q52R} channel has an open Kir6.2 inner helix gate (Fig. 4a). Clear cryoEM density shows rotation of the Kir6.2-F168 side chains away from the pore's center, thus causing a dilated pore size (Figs. 4a, 5a; Supplementary Fig. 4c; Supplementary movie 1). The radius of the K⁺ pathway at the inner helix gate is -3.3 Å, compared to -0.5 Å in the WT K_{ATP} channel bound to inhibitors we reported previously^{38,40}, exemplified by the ATP and repaglinide (RPG) bound structure (PDB ID 7TYS)³⁸ (Fig. 4b, c). The radius at the inner helix gate in our current structure is comparable to that in the open structure of SUR1/Kir6.2^{C166S,G334D} (3.3 Å)²⁸, and the pre-open structure of SUR1-Kir6.2^{H175K} fusion channel (3.0 Å)²⁹ (Fig. 4c). In contrast to the inner helix gate, little difference is observed in the G-loop gate between closed and open structures (Fig. 4), suggesting minimum involvement of the G-loop gate in K_{ATP} channel gating by PIP₂.

The SUR1/Kir6.2^{Q52R} K_{ATP} sample was purified in the absence of nucleotides; as expected, no ATP cryoEM density was observed at the inhibitory ATP-binding site on Kir6.2^{Q52R}. Nonetheless, the open conformation includes structural rearrangements at the ATP binding site that would disfavor ATP binding (Fig. 5a, c and Supplementary Fig. 4c, e). Specifically, the sidechains of Kir6.2-K39 and R50 flip away from ATP-interacting positions, with the K39 sidechain now coordinating PIP₂ at the non-canonical site; moreover, the sidechain of Kir6.2-E51 forms a salt bridge with R54 to partially occlude the ATP binding pocket (Fig. 5c). Our observation agrees with previous hypotheses that the open channel conformation is not compatible with ATP binding at Kir6.2 and that ATP inhibits the channel by stabilizing the channel in a closed conformation¹⁶.

Relative to channels bound to inhibitors, in which the Kir6.2-CTD is predominantly positioned close to the plasma membrane ("CTD-up" conformation)³⁸, the PIP₂-bound SUR1/Kir6.2^{Q52R} open channel structure shows the Kir6.2-CTD is also juxtaposing the membrane but further rotated clockwise (viewed from the extracellular side) (compare Fig. 5a and b; Supplementary movie 1). This twisting as well as the other structural changes at the ATP binding site discussed above are similarly observed in the open structure of the SUR1/Kir6.2^{C166S,G334D} channel²⁸, and the pre-open structure of the SUR1-Kir6.2^{H175K} fusion channel²⁹ (Supplementary Fig. 4d, f). The converging observations in three open structures using different mutant constructs suggest WT K_{ATP} channels undergo similar conformational changes between closed and open states.

Analysis of SUR1 structure

In the PIP₂-bound open SUR1/Kir6.2^{Q52R} structure, the two NBDs of SUR1 are not well resolved; in particular, NBD2 is highly dynamic with a local resolution > 5 Å (Fig. 1 and Supplementary Fig. 1d). However, the two NBDs are clearly separated, as predicted since no MgATP or MgADP was added to the sample. Notably, no cryoEM density corresponding to the distal N-terminal peptide of Kir6.2^{Q52R} was observed in the central cleft lined by TM helices from TMD1 and TMD2 of the SUR1-ABC core, even when the map was filtered to 7 Å (Supplementary Fig. 5a); no continuous density corresponding to KNtp was observed at an alternative site to suggest a stable resting position, precluding structural modeling of this flexible domain. The absence of KNtp cryoEM density in the PIP₂-bound open SUR1/Kir6.2^{Q52R} structure is in contrast to the clear KNtp density observed in the central cleft of SUR1-ABC core in the apo closed SUR1/Kir6.2^{Q52R} structure at comparable resolution and contour level (Supplementary Figs. 2e, 5b). Presence of KNtp in the SUR1-ABC core has been previously reported in inhibitor-bound structures and linked to channel closure^{38,41,42}. Worth noting, in a published open K_{ATP} structure where NBDs are bound to MgATP/MgADP and dimerized, KNtp density was also absent²⁸. The lack of KNtp in the SUR1-ABC core in the PIP₂-bound open SUR1/Kir6.2^{Q52R} structure further enforces the correlation between the absence of KNtp in the

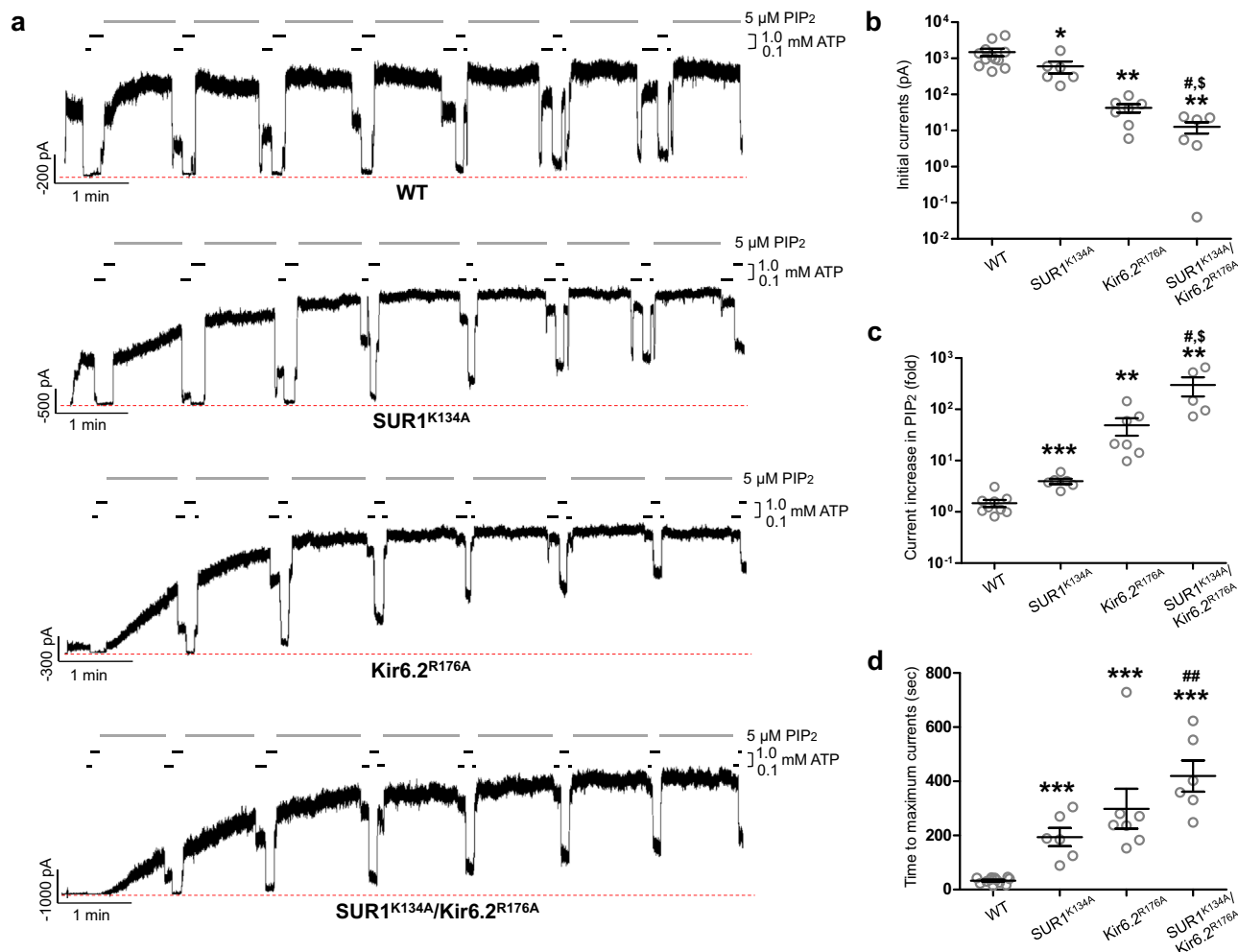


Fig. 3 | Functional testing of the two PIP₂ binding sites. **a** Representative inside-out patch-clamp recordings (−50 mV, inward currents shown as upward deflections; the red dashed line indicates 0 currents) of various channels: WT, SUR1^{K134A} (the non-canonical PIP₂ binding site mutation)/Kir6.2, SUR1^{K134A}/Kir6.2^{R176A} (the canonical PIP₂ binding site mutation), and SUR1^{K134A}/Kir6.2^{R176A} double mutant, exposed alternately in 5 μM PIP₂, 0.1 mM ATP, and 1 mM ATP as indicated by the bars above the recordings. The brief exposures to 0.1 mM and 1 mM ATP between PIP₂ exposures were used to monitor the gradual decrease in ATP sensitivity as channel opening became increasingly stabilized by PIP₂. **b** Group data of recordings shown in (a) comparing initial currents in K-INT at the time of patch excision. For each group, mean ± SEM of the data points are shown (WT, *n* = 12; SUR1^{K134A}, *n* = 6; Kir6.2^{R176A}, *n* = 7; SUR1^{K134A}/Kir6.2^{R176A}, *n* = 6 cells). Statistical significance was tested between mutants and WT or between double and single mutants using two-tailed unpaired *t* test with Welch's correction, alpha = 0.05. *SUR1^{K134A} vs WT, *p* = 0.0468; ** Kir6.2^{R176A} vs WT, *p* = 0.0016; **SUR1^{K134A}/Kir6.2^{R176A} vs WT, *p* = 0.0014; #SUR1^{K134A}/Kir6.2^{R176A} vs SUR1^{K134A}, *p* = 0.0440; \$SUR1^{K134A}/Kir6.2^{R176A} vs Kir6.2^{R176A}, *p* = 0.0411.

Note the y-axis in this panel and panel (c) is in log scale for better visualization. **c** Comparison of the maximum fold-increase in currents after PIP₂ exposure in different channels. For each group, mean ± SEM of the data points are shown (WT, *n* = 12; SUR1^{K134A}, *n* = 6; Kir6.2^{R176A}, *n* = 7; SUR1^{K134A}/Kir6.2^{R176A}, *n* = 5 cells). Statistical significance was tested between mutants and WT or between double and single mutants using two-tailed unpaired *t* test, alpha = 0.05. ***SUR1^{K134A} vs WT, *p* < 0.0001; ** Kir6.2^{R176A} vs WT, *p* = 0.0029; **SUR1^{K134A}/Kir6.2^{R176A} vs WT, *p* = 0.0012; #SUR1^{K134A}/Kir6.2^{R176A} vs SUR1^{K134A}, *p* = 0.0247; \$SUR1^{K134A}/Kir6.2^{R176A} vs Kir6.2^{R176A}, *p* = 0.0353. **d** Comparison of the time of exposure in PIP₂ for currents to reach maximum in different channels. For each group, mean ± SEM of the data points are shown (WT, *n* = 12; SUR1^{K134A}, *n* = 6; Kir6.2^{R176A}, *n* = 7; SUR1^{K134A}/Kir6.2^{R176A}, *n* = 6 cells). Statistical significance was tested between mutants and WT or between double and single mutants using two-tailed unpaired *t* test, alpha = 0.05. ***SUR1^{K134A} vs WT, *p* < 0.0001; ***Kir6.2^{R176A} vs WT, *p* = 0.0002; ***SUR1^{K134A}/Kir6.2^{R176A} vs WT, *p* < 0.0001; #SUR1^{K134A}/Kir6.2^{R176A} vs SUR1^{K134A}, *p* = 0.0071.

central cleft of the SUR1-ABC core and channel opening, whether SUR1 NBDs are dimerized or not.

The ABC modules of the four SUR1 subunits in the PIP₂-bound open SUR1/Kir6.2^{Q52R} map from a C4 non-uniform refinement adopt a propeller-like conformation (Fig. 1a, b). Further 3D classification of the symmetry-expanded particle set revealed three distinct rotational positions of the SUR1-ABC module relative to the Kir6.2/SUR1-TMD0 tetrameric core (Supplementary Fig. 6a, b). Similar conformational dynamics have been reported for the SUR1 NBDs-dimerized, open structure of the SUR1/Kir6.2^{C166S,G334D} channel²⁸, thus likely represent intrinsic flexibility of this domain regardless of nucleotide binding and/or NBD dimerization. In addition to the dynamics of the SUR1-ABC module within the PIP₂-bound open SUR1/Kir6.2^{Q52R} conformation

class, more pronounced heterogeneity was also captured in 3D classification of symmetry expanded particles that include all particles from 2D classes (Supplementary Fig. 2). Here, rotation of the SUR1-ABC module is seen correlated with the corkscrew position of the Kir6.2-CTD, with the SUR1-ABC module rotated in towards the Kir6.2 tetramer in the apo closed CTD-down conformation class, and more flung out in the PIP₂-bound open CTD-up conformation (Supplementary Figs. 2c, d and 6c, d). Such correlated dynamic movements of SUR1 and Kir6.2 may reflect the conformational transition between closed and open channels.

Compared to inhibitor-bound closed Kir6.2/SUR1 channel structures (reviewed in^{6,7}), SUR1 subunits in the PIP₂-bound SUR1/Kir6.2^{Q52R} open structure are more tilted away from Kir6.2 and elevated towards

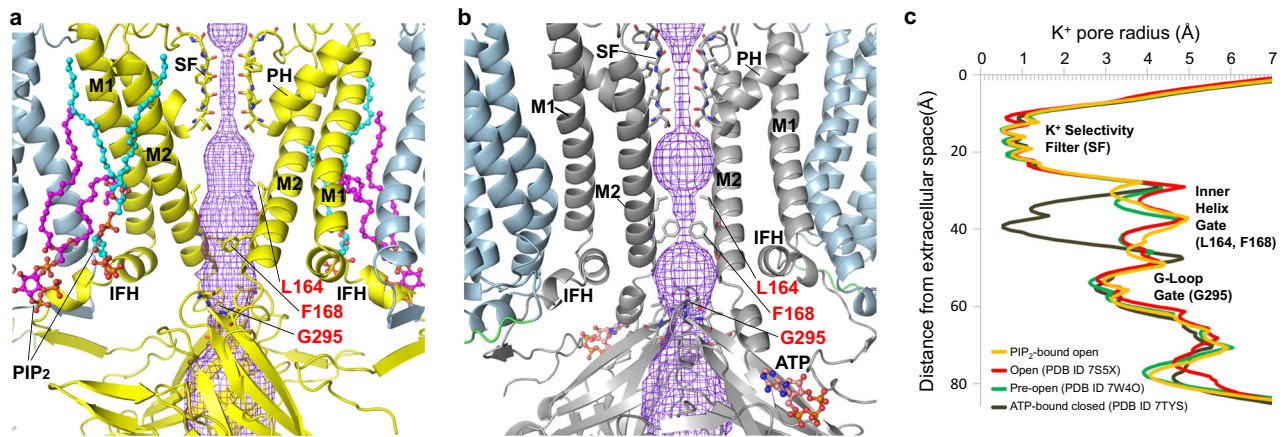


Fig. 4 | Comparison of the inner helix gate in the open and closed K_{ATP} channel structures. **a** View of the Kir6.2^{Q52R} pore in the PIP₂-bound SUR1/Kir6.2^{Q52R} open structure. Bound PIP₂ molecules are shown as cyan and magenta sticks and spheres, and the side chains of Kir6.2^{Q52R} inner helix gating residues L164 and F168 at the helix bundle crossing and G295 at the G-loop are shown as yellow sticks and labeled in red. The pore for the ion pathway (purple mesh) is constricted at the selectivity filter (SF) but open at the inner helix gate (3.3 Å). The Kir6.2^{Q52R} transmembrane α-

helices (M1 and M2), the interfacial α-helices (IFH) and the pore α-helices (PH) are labeled. **b** Kir6.2 in an ATP-bound closed state (PDB ID 6BAA) with similar labels as panel a for comparison. **c** Pore radii for ion conduction pathway plotted against the distance from the extracellular opening, with the location of the selectivity filter (residues 130–133), the inner helix gate (residues L164 and F168), and the G-loop gate (residues 294–297) shown. The pore radii were calculated using the program HOLE implemented in Coot and viewed using a MOLE rendering in PyMOL.

the plasma membrane (viewed from the side) such that they are nearly in plane with the Kir6.2 tetramer (compare Fig. 1b and c). Accompanying this upward SUR1 motion, there is an overall rigid-body rotation of SUR1 driven by a rotation of the TMD0 of SUR1 in the open structure relative to closed structures (Fig. 6). At the outer leaflet, SUR1-F41, which interacts with Kir6.2-L84 in the closed conformation, now interacts with Kir6.2-L85 in the open conformation (Fig. 6c). At the inner leaflet, SUR1-TMD0 moves away from Kir6.2 (Fig. 6a, c), creating a space between SUR1-TM1 and Kir6.2-M1. Using PISA analysis⁴³, the contact surface area at this interface (between SUR1-TM1 residues 27–54 and Kir6.2-M1 residues 66–96) is 645.6 Å² ($\Delta G = -20$ kcal/mol) in the closed channel structure (PDB ID 6BAA), which is reduced to 395.9 Å² ($\Delta G = -12$ kcal/mol) in the PIP₂-bound SUR1/Kir6.2^{Q52R} open structure. Binding of a second PIP₂ in this space, i.e. the non-canonical PIP₂ binding site (see Fig. 2b), compensates for the lost surface contact between SUR1-TMD0 and Kir6.2, thus stabilizing this interface in the open channel.

Similar structural changes were also described in the pre-open SUR1-Kir6.2^{H175K} fusion structure where SUR1 NBDs are bound to MgATP/MgADP and dimerized³⁰ (Supplementary Fig. 4). Dimerization of SUR1 NBDs antagonizes ATP inhibition at Kir6.2 and stimulates K_{ATP} channel activity. It has been proposed that NBD dimerization causes outward bending of the cytoplasmic half of SUR1-TMD0 and the pulling away of K205 in SUR1-LO from binding ATP at the inhibitory site to stimulate channel activity³⁰. Since our PIP₂-bound open SUR1/Kir6.2^{Q52R} structure does not contain MgATP/MgADP and the NBDs are clearly separated, the similar conformational changes we observed at SUR1-TMD0/LO are not driven by SUR1 NBD dimerization. One possibility is that MgATP/MgADP and PIP₂ converge on the same structural mechanism to open the channel, as has been proposed previously based on functional studies⁴⁴.

Kir6.2-Q52R stabilizes the open conformation by interacting with SUR1-W51

Kir6.2-Q52 is located immediately N-terminal to the interfacial helix (IFH; a.k.a. slide helix) and C-terminal to βA (Fig. 5c, d). In published ATP-bound closed structures, Kir6.2-Q52 lies close to SUR1-E203 in the proximal portion of the SUR1-LO linker (Fig. 5d). Previous studies have shown that enforcing Kir6.2-Q52 and SUR1-E203 interactions via engineered charged amino acid pair or cysteine crosslinking reduced ATP inhibition IC₅₀ by 100-fold or caused spontaneous channel closure

in the absence of ATP, respectively⁴⁵. These results indicate that stabilizing the interface between Kir6.2 βA-IFH and SUR1-LO stabilizes ATP binding and channel closure. In contrast, in the PIP₂-bound SUR1/Kir6.2^{Q52R} open structure, the SUR1-LO linker moves -7 Å towards SUR1 and away from the ATP-binding site on Kir6.2 (compare Fig. 5c and d), with SUR1-E203 and K205 flipped away from Kir6.2 such that SUR1-TMD0 ICL1 (aa 52–60) engages with Kir6.2-βA to form a main chain β-sheet (Fig. 5c). In particular, the sidechain of Kir6.2 residue 52 (Q in WT, R in the mutant) now faces SUR1-TMD0 and interacts with SUR1-W51 (Fig. 5c and Supplementary Fig. 4e), tethering the Kir6.2-CTD to SUR1-TMD0 in a rotated open position.

The Kir6.2-Q52R mutation increases P_o and decreases ATP inhibition of K_{ATP} channels in a SUR1-dependent manner⁴⁶. The cation-π interaction observed between Kir6.2-Q52R and SUR1-W51 in the open conformation (Fig. 7a) led us to hypothesize that this interaction may contribute to the gain-of-function gating effect of the Kir6.2-Q52R mutation, by stabilizing the Kir6.2-CTD in a rotated open conformation. To test this, we mutated W51 of SUR1 to cysteine and assessed the ATP sensitivity of channels formed by co-expressing Kir6.2^{Q52R} and SUR1^{W51C} using inside-out patch-clamp recording. SUR1^{W51C} reversed the effect of Kir6.2^{Q52R} such that the ATP sensitivity of the channel resembles WT channels (Fig. 7b). The IC₅₀ values of ATP inhibition for WT, SUR1/Kir6.2^{Q52R}, SUR1^{W51C}/Kir6.2, and SUR1^{W51C}/Kir6.2^{Q52R} channels are 6.25 ± 0.44 μM, 161.2 ± 16.23 μM, 20.88 ± 1.96 μM, and 8.98 ± 0.49 μM, respectively (Fig. 7c). Corroborating these findings, in Rb⁺ efflux assays cells co-expressing Kir6.2^{Q52R} and SUR1^{W51C} showed efflux levels similar to cells expressing WT channels, in contrast to the significantly higher efflux in cells co-expressing Kir6.2^{Q52R} and WT-SUR1 (Fig. 7d). These results provide strong evidence that Kir6.2-Q52R interacts with SUR1-W51 to enhance channel activity and reduce ATP inhibition, thus providing an explanation for the SUR1-dependent pathophysiology of this neonatal diabetes mutation.

To test whether the interaction between Kir6.2-Q52R and SUR1-W51 that gives rise to the enhanced activity and reduced ATP sensitivity is dependent on PIP₂ binding at the two adjacent sites revealed by our structure, we determined the effect of Kir6.2^{Q52R} on the background of SUR1^{K134A}, Kir6.2^{R176A}, or SUR1^{K134A} and Kir6.2^{R176A}, which weaken the non-canonical PIP₂ binding site, the canonical PIP₂ binding site, or both. Inside-out patch-clamp recording experiments showed a leftward shift in the dose response of ATP inhibition of the SUR1^{K134A}/Kir6.2^{Q52R} channel (IC₅₀ = 54.08 ± 7.14 μM, H = 1.55), the SUR1/

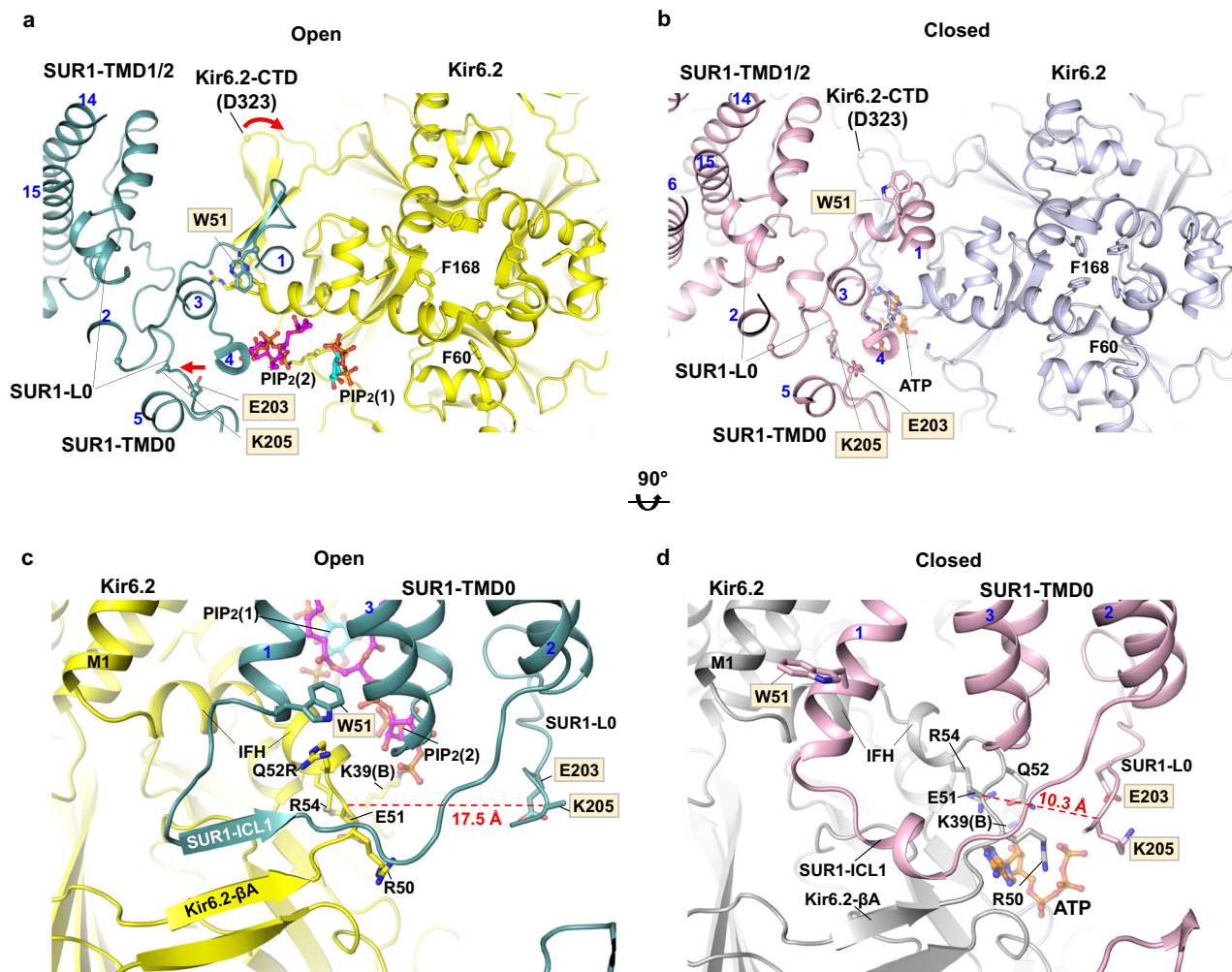


Fig. 5 | SUR1 and Kir6.2 cytoplasm-plasma membrane interface in open and closed K_{ATP} channel conformations. **a** SUR1-Kir6.2 cytoplasm-plasma membrane interface in open PIP₂ (cyan and magenta sticks)-bound SUR1/Kir6.2^{Q52R} (SUR1 in teal and Kir6.2 in yellow) structure, and **(b)** closed ATP- (orange carbon sticks) and repaglinide (out of view)-bound WT (SUR1 in pink and Kir6.2 in gray) K_{ATP} channel (PDB ID 7TYS) viewed from the extracellular side. Note reorientation of side chains of the Kir6.2 inner helix gate residue F168 and M1 residue F60, as well as W51 at the bottom of TMI of SUR1-TMD0 in the two conformations. In **(a)**, a 6.4° clockwise rotation of the Kir6.2-CTD comparing the open to the closed conformation is indicated by the red curved arrow (with D323 Cα in each structure marked as spheres), and SUR1-L0, marked by the ATP-binding residue K205 and an adjacent residue E203, movement away from the ATP binding pocket in the open

conformation relative to the closed conformation is marked by a red arrow. **c** A side view of the interface in the open conformation. SUR1-intracellular loop 1 (ICL1) forms a β-sheet with Kir6.2-βA just before the interfacial helix (IFH). Remodeling of residues involved in ATP binding and gating compared to the closed conformation in **(d)**, including Kir6.2-R50, R54, E51 and K39(B) (“B” denotes the adjacent Kir6.2 subunit) as well as SUR1-E203 and K205 in LO are shown. Most notably, the Kir6.2 mutant residue Q52R has its side chain reoriented to interact with the side chain of SUR1-W51 which also has its side chain reoriented with the closed conformation. Color scheme same as **(a)**. **d** The same side view as in **(b)** but of the closed conformation. In all panels, SUR1 residue labels are outlined in gray. The red dashed line in **(c)** and **(d)** is the distance between the Cα of Kir6.2 E51 and SUR1 K205. In all panels, SUR1 helices are indicated with blue numbers.

Kir6.2^{Q52R/R176A} channel ($IC_{50} = 17.97 \pm 1.20 \mu M$, $H = 1.41$), and the SUR1K^{134A}/Kir6.2^{Q52R/R176A} channel ($IC_{50} = 8.30 \pm 1.11 \mu M$, $H = 1.18$) relative to the SUR1/Kir6.2^{Q52R} channel ($IC_{50} = 161.20 \pm 16.23 \mu M$, $H = 2.34$) (Supplementary Fig. 7a). SUR1^{K134A} or Kir6.2^{R176A} alone had little effect on the IC_{50} of ATP inhibition ($4.12 \pm 0.30 \mu M$, $H = 1.54$, and $11.27 \pm 1.95 \mu M$, $H = 0.84$, respectively, compared to $6.25 \pm 0.44 \mu M$, $H = 0.93$ for WT channels). In agreement, Rb⁺ efflux experiments showed attenuation of the gain-of-function phenotype associated with Kir6.2^{Q52R} when combined with PIP₂ binding mutations SUR1^{K134A}, Kir6.2^{R176A}, or both (Supplementary Fig. 7b). Taken together, these results support a role of PIP₂ at the two binding sites in manifesting the gain-of-function effect of Kir6.2^{Q52R}.

Discussion

In this study, we surmounted the technical difficulties in capturing PIP₂-bound to K_{ATP} channel, firstly by using a neonatal-diabetes Kir6.2

variant known to enhance channel activity, and secondly by using naturally occurring long-chain PIP₂ before membrane solubilization, rather than the previously used approach of adding short-chain synthetic diC8-PIP₂ after channel purification^{24,30,47}. The tandem PIP₂ binding site coordinated by Kir6.2 itself and its regulatory subunit SUR1 uncovers a cooperation between an ion channel and transporter on PIP₂ binding, and sets apart the K_{ATP} complex in the evolution of K⁺ channels and ABC proteins. The structure offers a resolution to a major problem in the long-standing puzzle of how SUR1, in particular TMD0 of SUR1, modulates the open probability of the Kir6.2 channel^{25,26}. Moreover, it suggests a molecular mechanism for how a prominent neonatal diabetes-causing Kir6.2 mutation increases channel activity⁴⁶.

Distinct PIP₂ binding pocket in K_{ATP} channels

As a member of the Kir channel family, Kir6.2 was expected to contain a canonical PIP₂ binding site, akin to that identified in Kir2 and Kir3^{17–20}.

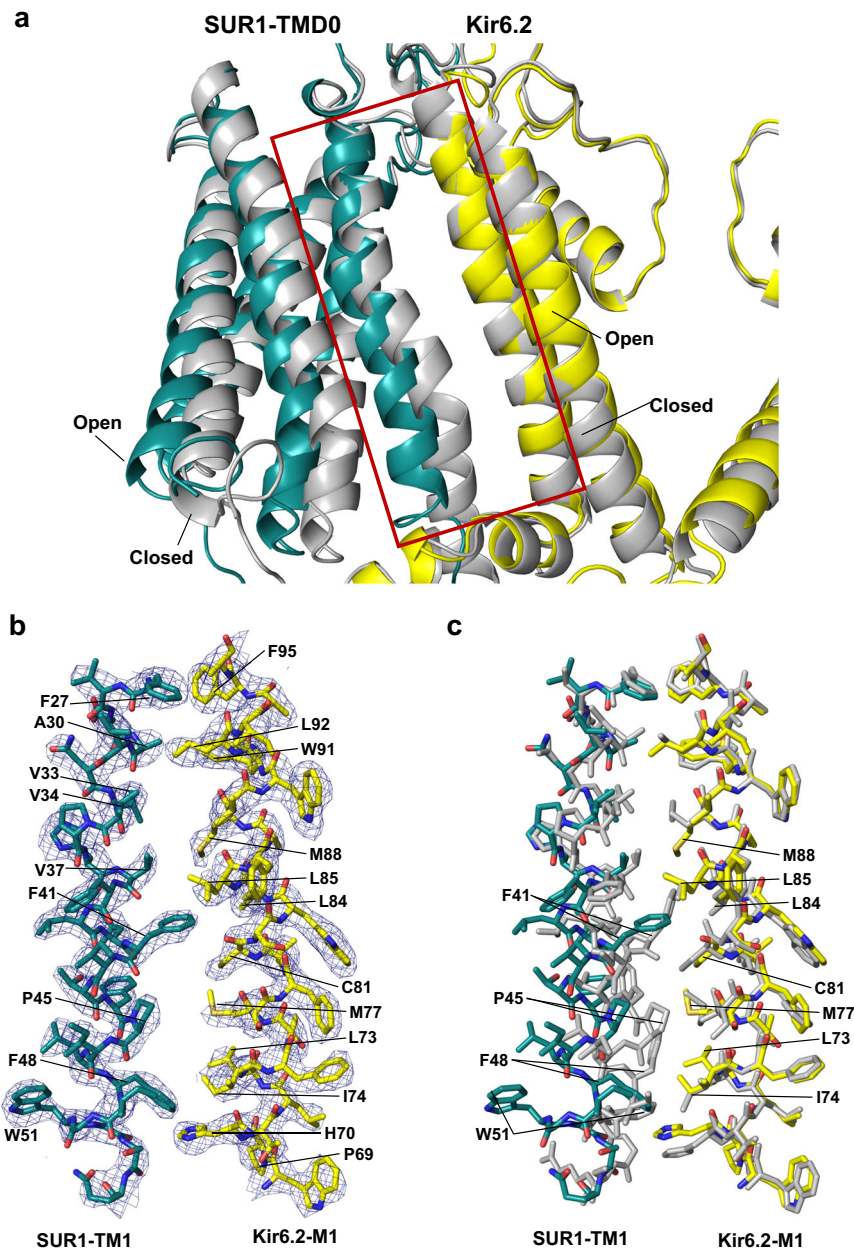


Fig. 6 | Structural changes between open- and closed-forms of the K_{ATP} channel at the SUR1 and Kir6.2 TM interface. **a** An overlay of the SUR1-Kir6.2 TM interface between the open SUR1/Kir6.2^{Q52R} K_{ATP} channel and the closed K_{ATP} channel (PDB ID 6BAA) showing the outward movement of the cytoplasmic half of the SUR1-TMD0. In the open structure, SUR1 is shown in teal and Kir6.2 in yellow. The closed structure is shown in gray. **b** Close-up view of the open structure in the boxed

region in (a). CryoEM map (blue mesh, 0.17 V/8.5 σ map contour) is superposed with the structural model. For clarity, PIP₂ is omitted. **c** An overlay of the open with the closed K_{ATP} channel structures in the boxed region in (a) (same color scheme) showing significant changes in residues of SUR1-TM1 at the inner leaflet half of the plasma membrane.

Our structure confirms that this is indeed the case. Surprisingly, our structure reveals a second, non-canonical PIP₂ binding site immediately next to the conserved canonical Kir channel PIP₂ binding site. This non-canonical site is coordinated by both SUR1 and Kir6.2 subunits. Mutational studies support functional importance of PIP₂ binding at both sites (Fig. 3). In single channel recordings, Kir6.2 channels lacking SUR1 have low P_o with brief openings, in contrast to Kir6.2 channels assembled with SUR1 or SUR1-TMD0, which exhibit ~10-fold higher P_o and long bursts of openings^{16,25,26,48}. We propose the low P_o and brief openings in Kir6.2 channels lacking SUR1 result from PIP₂ binding at the canonical site, which tethers the Kir6.2-CTD near the membrane to rotate to the open position. PIP₂ binding at this site may not be as strong as in Kir2 and Kir3 channels due to sequence variations

at key residues including Kir6.2 P69 and H175 (both positively charged amino acids in Kir2 and 3)^{17–20}, explaining the low P_o of Kir6.2. PIP₂ binding at the non-canonical site formed by SUR1 and Kir6.2 enables SUR1 to stabilize the Kir6.2-CTD in the rotated open position, giving rise to bursts of openings and higher P_o .

The space between Kir6.2 and SUR1-TMD0 in the previously published inhibitor-bound closed structure is more constricted than that in the PIP₂-bound SUR1/Kir6.2^{Q52R} open structure. In a solvent-accessible surface representation of the model for a closed structure (exemplified by the repaglinide/ATP bound PDB ID 7TYS)³⁸, PIP₂ at the non-canonical site would clash with SUR1 (Supplementary Fig. 8b). Inspection of the closed SUR1/Kir6.2^{Q52R} CTD-down conformation (see Supplementary Fig. 2) also finds that PIP₂ binding at the non-canonical

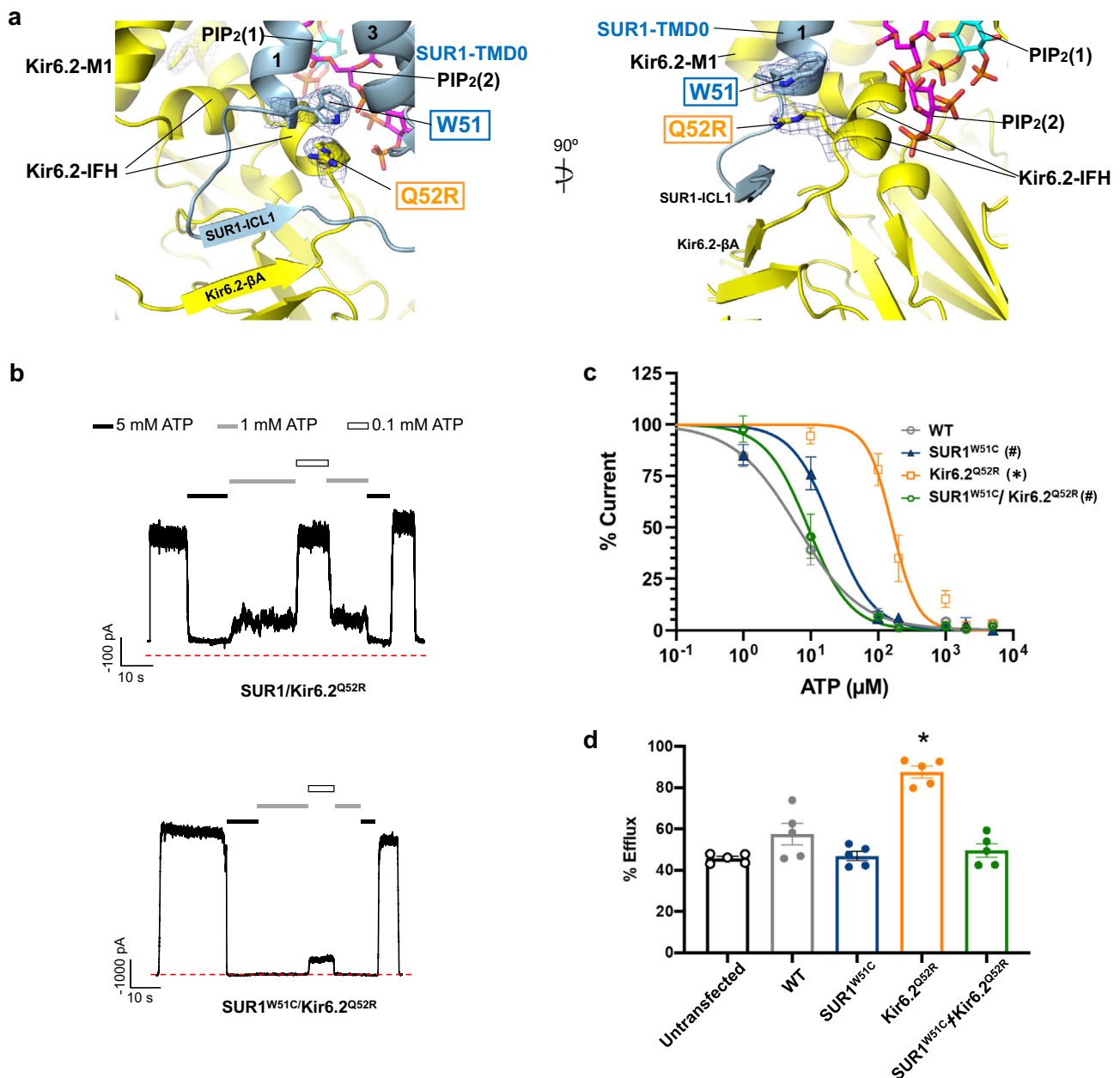


Fig. 7 | Kir6.2-Q52R interacts with SUR1-W51 to reduce channel sensitivity to ATP inhibition and enhance channel activity. **a** A close-up view of the interaction between Kir6.2-Q52R and SUR1-W51 with cryoEM map (blue mesh, 0.17 V/8.5 σ contour) superposed with the structural model in two different angles. **b** Representative inside-out patch-clamp recordings (-50 mV, inward currents shown as upward deflections; red dashed lines mark baseline 0 currents) of the SUR1/Kir6.2^{Q52R} channel and SUR1^{W51C}/Kir6.2^{Q52R} channel exposed to differing concentrations of ATP as indicated by the bars above the recordings. **c** ATP dose response of WT (SUR1/Kir6.2) channels, channels containing the SUR1^{W51C} mutation (SUR1^{W51C}), Kir6.2^{Q52R} mutation (Kir6.2^{Q52R}), or both SUR1^{W51C} and Kir6.2^{Q52R} mutations (SUR1^{W51C}/Kir6.2^{Q52R}). Curves were obtained by fitting the data points to the Hill equation (see Methods). Each data point is shown as mean \pm SEM (error bar) of WT, $n = 3, 8, 5, 5, 3, 4, 3$ cells for 1 μ M, 10 μ M, 100 μ M, 200 μ M, 1 mM, 2 mM, 5 mM,

respectively; SUR1^{W51C}, $n = 3, 4, 7, 5, 3, 5, 3$ cells for 1 μ M, 10 μ M, 100 μ M, 200 μ M, 1 mM, 2 mM, 5 mM, respectively; Kir6.2^{Q52R}, $n = 7, 8, 7, 3, 7, 3$ cells for 10 μ M, 100 μ M, 200 μ M, 1 mM, 2 mM, 5 mM, respectively; SUR1^{W51C}/Kir6.2^{Q52R}, $n = 3, 7, 5, 3, 9, 3, 4$ cells for 1 μ M, 10 μ M, 100 μ M, 200 μ M, 1 mM, 2 mM, 5 mM, respectively. Statistical significance in IC₅₀ was tested using one-way ANOVA with Tukey's post hoc test, $\alpha = 0.05$. * $p < 0.0001$, Kir6.2^{Q52R} vs WT; # $p < 0.0001$, SUR1^{W51C} and SUR1^{W51C}/Kir6.2^{Q52R} vs Kir6.2^{Q52R}. **d** Rb⁺ efflux of various channels (same labeling as in **c**) expressed in COSm6 cells. Untransfected cells were included to show background efflux. Each bar represents means \pm SEM of $n = 5$ independent experiments. Statistical significance test using one-way ANOVA shows means are significantly different ($p < 0.0001$, $\alpha = 0.05$). Tukey's post hoc test shows only SUR1/Kir6.2^{Q52R} is significantly different from WT, * $p < 0.0001$.

site would clash with SUR1 (Supplementary Fig. 8c), indicating this structure represents an apo state, at least with respect to PIP₂ binding at the non-canonical site. These observations imply that PIP₂ moves in and out of the second site as the channel opens and closes. In this regard, it is interesting to note that a conformation-dependent change in the PIP₂ binding site in the voltage-dependent KCNQ1 (Kv7.1) channel was recently reported, where the movement of the voltage

sensing transmembrane helix S4 up or down the membrane is associated with opening or occlusion of the PIP₂ binding site to open or close the channel, respectively⁴⁹. In our published closed structures without exogenous PIP₂, there was also lipid density, which we tentatively modeled as two phosphatidylserines³⁸. Due to resolution differences, it is not possible to resolve lipid density in the apo closed SUR1/Kir6.2^{Q52R} channel map. Whether other smaller lipids may occupy

the space vacated due to incompatibility of PIP₂ binding at the remodeled non-canonical site in closed channel conformations as channels open and close remains to be determined. Further studies are also needed to determine whether the canonical PIP₂ binding site is always occupied by PIP₂ since it appears available in both the open and closed channel conformations (Supplementary Fig. 8).

K_{ATP} channels exhibit lower specificity towards PIPs compared to other Kir channels, and are activated equally well by PI(4,5)P₂, PI(3,4)P₂, and PI(3,4,5)P₃, and also by PI(4)P and long chain (LC)-CoAs³³. The structural basis underlying the reduced PIPs specificity for K_{ATP} channel activation requires further investigation, but the large size of the binding pocket may accommodate different PIPs and LC-CoAs. Such degeneracy may account for the observation that purified K_{ATP} channels reconstituted in lipid bilayers lacking PIP₂ exhibited spontaneous single channel openings²⁸, in contrast to Kir2 and Kir3 channels which require PIP₂ for activity^{20,50}.

Mechanism of PIP₂ and ATP antagonism

PIP₂ and ATP functionally compete to open or close K_{ATP} channels (Fig. 3a)^{11,12}. Kinetic analyses have indicated that PIP₂ and ATP binding are mutually excluded¹⁶. Comparison between the PIP₂-bound SUR1/Kir6.2^{Q52R} open structure and previously published ATP-bound closed structures shows PIP₂ and ATP antagonism occurs via both binding competition and allosteric mechanisms (Fig. 5 and Supplementary movie 1). At the level of binding competition, both ligands compete for a common binding residue, Kir6.2-K39, which interacts with ATP in the ATP-bound closed structures^{38,40} but with PIP₂ in the PIP₂-bound open structure (Figs. 2b and 5c). Previous molecular dynamics simulations, using ATP-bound closed structures of Kir6.2 tetramer⁵¹ or tetramer of Kir6.2 plus SUR1-TMDO³⁸ with a single PIP₂ molecule docked in the canonical PIP₂ binding site, found that Kir6.2-K39⁵¹ or both K39 and R54³⁸ switched between ATP binding and PIP₂ binding. In the PIP₂-bound SUR1/Kir6.2^{Q52R} open structure, we see Kir6.2-K39, rather than binding PIP₂ in the canonical site, binds the second PIP₂ in the non-canonical site. In contrast, Kir6.2-R54 does not appear to be involved in PIP₂ binding; instead, it interacts with Kir6.2-E51 in the same subunit and E179 in the adjacent Kir6.2 subunit, which stabilizes the interface between the IFH and the C-linker helix (the linker helix connecting M2 and C-terminal cytoplasmic domain of Kir6.2) in the open conformation. Mutation of both K39 and R54 to alanine has been shown to reduce ATP as well as PIP₂ sensitivities⁵². Our structure clarifies the structural role of K39 and R54 and suggests while K39A likely reduces PIP₂ sensitivity by weakening PIP₂ binding at the non-canonical site, R54A may reduce PIP₂ sensitivity indirectly by disrupting interactions in Kir6.2 that are needed to stabilize the open channel conformation.

Allosterically, PIP₂ binding diverts ATP binding residues away from the ATP binding pocket to disfavor ATP binding. These include sidechain reorientation of Kir6.2 K39 and R50, and interaction between Kir6.2 R54 and E51 that partially occludes the ATP binding pocket (Fig. 5c). Moreover, in the ATP-bound closed conformation, SUR1-L0 interfaces with Kir6.2-βA, allowing SUR1-K205 to coordinate ATP binding^{38,42,45,53} and stabilize channel closure. However, in the PIP₂-bound open SUR1/Kir6.2^{Q52R} structure, SUR1-L0 is disengaged from Kir6.2-βA, allowing Kir6.2-CTD to rotate such that ICL1 of SUR1-TMDO engages with Kir6.2-βA, forming a continuous β-sheet to stabilize the open conformation, which also disfavors ATP binding. Similar changes have been described in the published SUR1/Kir6.2^{C166S,C334D} open structure²⁸, and the SUR1-Kir6.2^{H175K} fusion pre-open structure³⁰ (Supplementary Fig. 4f). The common structural rearrangements from the closed to the open state are independent of mutations, which suggests the same gating transition occurs in WT channels, and highlights a key role of SUR1 in stabilizing the Kir6.2-CTD in two distinct rotational positions to close or open the K_{ATP} channel.

Insights on disease mutations

This study sheds light on how the neonatal diabetes-associated Kir6.2^{Q52R} causes gain of K_{ATP} channel function. The strong cation-π interaction engendered by the Kir6.2-Q52R mutation with SUR1-W51 illustrates how changes at this interface have profound effects on channel gating and physiology. In the published SUR1/Kir6.2^{G334D,C166S} open structure and the SUR1-Kir6.2^{H175K} fusion channel pre-open structure Q52 of Kir6.2 is similarly in position to interact with W51 of SUR1^{28,29} (see Supplementary Fig. 4f). The polar-π interaction between glutamine and tryptophan is much weaker than the cation-π interaction between arginine and tryptophan. The difference in binding energy for the relevant gas-phase interactions for polar-π is 1.4 kcal/mol (NH₃-Benzene), compared to the cation-π interaction energy of 19.0 kcal/mol (NH₄⁺-Benzene)^{54,55}. That Q52 and Q52R in Kir6.2 both interact with W51 of SUR1 suggests an important role of Kir6.2-Q52 in stabilizing the Kir6.2-CTD and SUR1-TMDO interface for channel opening. Functional studies showing that weakening PIP₂ binding at either site attenuates both WT and SUR1/Kir6.2^{Q52R} activity are consistent with endogenous PIP₂ being important for the activity of both WT and mutant channels. In the absence of normal PIP₂ binding, the gain-of-function effect of Kir6.2^{Q52R} becomes much weaker. The presence of a minor conformation class corresponding to a closed SUR1/Kir6.2^{Q52R} channel with an occluded (apo) non-canonical PIP₂ binding site (Supplementary Figs. 2, 8c) in our sample further strengthens the notion that Kir6.2^{Q52R} alone is insufficient to support the open channel conformation in the absence of PIP₂.

In addition to Kir6.2^{Q52R}, many disease mutations are located at the SUR1-Kir6.2 interface seen in the PIP₂-bound SUR1/Kir6.2^{Q52R} open structure (Fig. 8). These include congenital hyperinsulinism (CHI) associated loss-of-function Kir6.2 mutations: R54C, L56G, K67D, R176H and R177W, and SUR1 mutations: I46T, P133R, and L135V as well as neonatal diabetes (ND) and Developmental delay, Epilepsy, and Neonatal Diabetes (DEND) syndrome associated gain-of-function Kir6.2 mutations: K39R, E51A/G, Q52L/R, G53D/N/R/S/V, V59A/G/M, W68C/G/L/R, K170N/R/T, E179A/K, and SUR1 mutations: P45L, I49F, F132L/V, and L135P (Fig. 8)⁵⁶. Some of these, such as CHI-associated K67D and R176H, and ND/DEND associated K39R, W68C/G/L/R involve residues that coordinate PIP₂ binding; others, however, likely affect PIP₂ or ATP gating allosterically by stabilizing channels in closed or open conformations.

In summary, the PIP₂-bound K_{ATP} channel structure elucidates the intimate partnership between SUR1 and Kir6.2 in coordinating PIP₂ binding and channel gating. The PIP₂ binding pocket and the molecular interactions involved in gating identified here provide a framework for designing new K_{ATP} modulators to control channel activity. The finding that SUR1 binds PIP₂ to regulate Kir6.2 also raises the question of whether PIP₂ serves structural and functional roles in other ABC proteins, as has been implicated for CFTR⁵⁷.

Methods

Cell lines

COSm6 cells (RRID:CVCL_8561) were used for K_{ATP} channel expression. HEK-AD293 cells (RRID:CVCL_0063; from Agilent Technologies catalog number 240085) were used for production of recombinant adenoviruses encoding FLAG-SUR1 and Kir6.2^{Q52R}. Both COSm6 and HEK-AD293 cells were cultured in high-glucose DMEM medium (GIBCO) supplemented with 10% Fetal Bovine Serum (Fisher Scientific), 100 U/mL penicillin, and 100 U/mL streptomycin at 37 °C with 5% CO₂.

Protein expression and purification

Genes encoding rat Kir6.2^{Q52R} and N-terminal FLAG-tagged (DYKDDDDK) hamster SUR1 were cloned into pShuttle vectors and then the AdEasy vector, and packaged into recombinant adenoviruses in HEK-AD293 cells according to manufacturer's instructions (<https://www.agilent.com/cs/library/usermanuals/public/240009.pdf>).

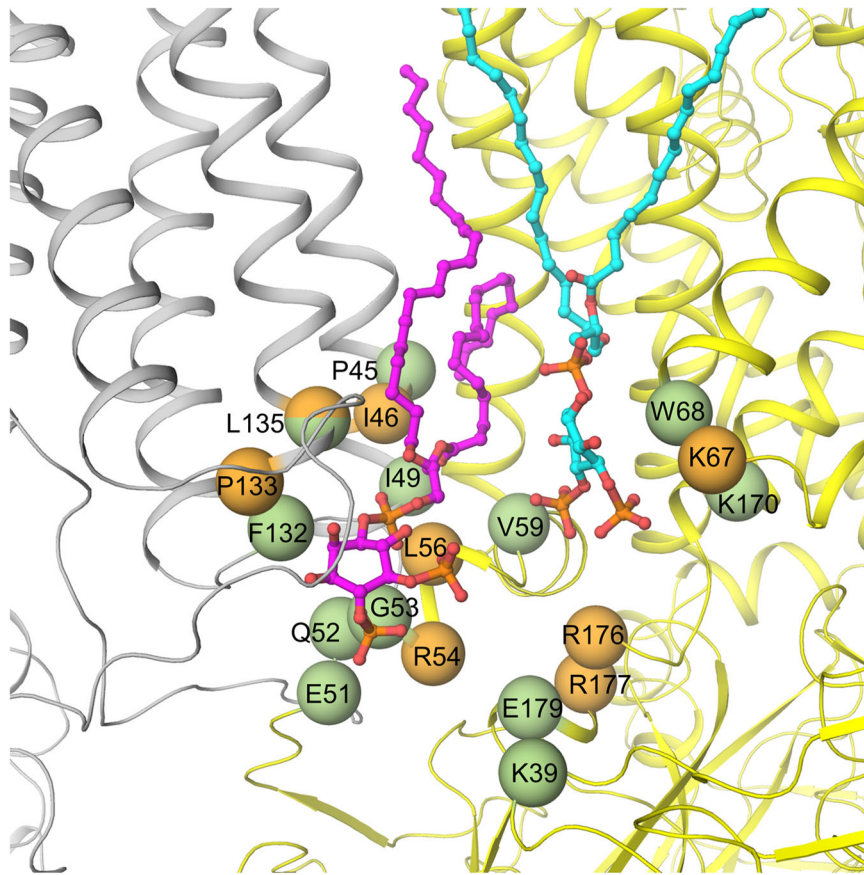


Fig. 8 | K_{ATP} channel disease mutations near the PIP_2 binding pocket. Residues with variants that have been reported to cause neonatal diabetes/DEND syndrome are shown as green spheres and congenital hyperinsulinism shown as orange spheres (with the exception of L135, which is colored half green and half orange as mutation at this position has been linked to both diseases depending on the

substituting amino acid). Neonatal diabetes/DEND syndrome mutations include SUR1-P45L, I49F, F132L/V, L135P, and Kir6.2-K39R, E51A/G, Q52L/R, G53D/N/R/S/R/V, V59A/G/M, W68C/G/L/R, K170N/R/T, E179A/K. Congenital hyperinsulinism mutations include SUR1-I46T, P133R and L135V, and Kir6.2-R54C, L56G, K67D, R176H, and R177W. SUR1 and Kir6.2 are colored gray and yellow, respectively.

Purified recombinant adenoviruses were used to transduce COSm6 cells for protein expression⁵⁸. COSm6 cells grown to mid-log in 15 cm tissue-culture plates were transduced with adenoviruses packaged with Kir6.2, SUR1, and tTA, using multiplicity of infections (MOIs) optimized empirically. Note the pShuttle vector used for SUR1 contains a tetracycline-regulated response element, necessitating co-transduction of a tTA (tetracycline-controlled transactivator) adenovirus for SUR1 expression. At -24 h post-transduction, cell medium was changed and 100 μ M tolbutamide was added to the medium to enhance K_{ATP} channel assembly and expression at the plasma membrane⁵⁹. At -48 h post-transduction, cells were harvested by scraping and cell pellets were frozen and stored at -80 °C until purification.

For SUR1/Kir6.2^{Q52R} channel purification, cells were resuspended in hypotonic buffer [15 mM KCl, 10 mM HEPES, 0.25 mM dithiothreitol (DTT), pH 7.5] and lysed with a tight-fitting Dounce homogenizer, then centrifuged at 20,000xg for 60 min. The spun-down materials, which include membranes, were re-suspended in buffer containing 0.2 M NaCl, 0.1 M KCl, 0.05 M HEPES pH 7.5, 4% trehalose, and 1 mg/mL brain PIP_2 (Avanti Polar Lipids, catalog number 840046), and incubated at 4 °C for 30 min before increasing the volume 10x in the same buffer without added lipids but including the detergent digitonin at a final concentration of 0.5%, then membranes were solubilized at 4 °C for 90 min. Solubilized membranes were separated from insoluble materials by centrifugation (100,000xg for 30 min at 4 °C). The soluble fraction was incubated with anti-FLAG M2 affinity agarose for 10 h and eluted at 4 °C for 60 min with a buffer containing 0.2 M NaCl, 0.1 M

KCl, 0.05 M HEPES pH 7.5, 0.05% digitonin and 0.25 mg/mL FLAG peptide. Purified channels were eluted at -170 nM (-150 μ g/ml) and used immediately for cryo-EM grid preparation. K_{ATP} channel particles were also fixed and stained using Uranyl Acetate and sample quality was assessed by negative-stain-EM.

CryoEM sample preparation and data acquisition

To increase protein adsorption to the cryoEM grids, and also to mitigate selective-orientation of K_{ATP} channel particles that occurs on commercial carbon surfaces, graphene-oxide (GO) grids were prepared as follows⁵⁸. Gold Quantifoil RL2/1.3 400 mesh grids were cleaned with acetone and glow-discharged for 60 s at 15 mA with a Pelco EasyGlow[®], and 4 μ L of 1 mg/mL Polyethylenimine (PEI, 40,000 molecular weight) in 25 mM HEPES pH 7.9 was applied to each grid and incubated for 2 min followed by washing with water. Then, 0.1 mg/ml GO was vortexed vigorously and applied to the grid and incubated for 2 min followed by two washes with water. The GO grids were allowed to dry for 15 min and used within 2 h for sample vitrification.

To prepare cryoEM samples, 3 μ L of purified K_{ATP} channel complex was loaded onto fresh GO-coated grids for 30 s at 6 °C with a humidity of 100%. Grids were blotted for 2.5 s with a blotting force of -10 and cryo-plunged into liquid ethane cooled by liquid nitrogen using a Vitrobot Mark III (FEI).

Single-particle cryo-EM data was collected on a Titan Krios 300 kV cryo-electron microscope (ThermoFisher Scientific) in the Pacific Northwest CryoEM Center (PNCC), with a multi-shot strategy using beam shift to collect 27 movies per stage shift, assisted by the

automated acquisition program SerialEM. Images were recorded on the Gatan K3 Summit direct-electron detector in super-resolution mode, post-GIF (20 eV window), at 105,000x magnification (calibrated image pixel-size of 0.826 Å; super-resolution pixel size 0.413 Å); nominal defocus was varied between -1.0 and -2.5 μm across the dataset. The dose rate was kept around 24 $\text{e}/\text{\AA}^2/\text{s}$, with a frame rate of 35 frames/sec, and 78 frames in each movie (i.e. 2.2 s exposure time/movie), which gave a total dose of approximately 55 $\text{e}/\text{\AA}^2$. Three grids that were prepared in the same session using the same protein preparation were used for data collection, and from these three grids, 2727, 3956 and 1576 movies (8,259 movies total) were recorded.

CryoEM image processing

Super-resolution dose-fractionated movies were gain-normalized by inverting the gain reference in Y and rotating upside down, corrected for beam induced motion, aligned, and dose-compensated using Patch-Motion Correction in cryoSPARC v4.4.1 (hereinafter referred to as cryoSPARC)⁶⁰ without binning. Parameters for the contrast transfer function (CTF) were estimated from the aligned frame sums using Patch-CTF Estimation in cryoSPARC⁶⁰ and binned by 2 with Fourier cropping. Micrographs were manually curated using sorting by curate exposures. The resulting 5241 dose-weighted motion-corrected summed micrographs were used for subsequent cryo-EM image processing. Particles were picked automatically using template-based picking in cryoSPARC based on 2D classes obtained from cryoSPARC live during data collection. For each of the three sets of data, particles were cleaned by three rounds of 2D classification in cryoSPARC⁶⁰. The combined particle stack contained 70,638 particles, which were then used for ab initio reconstruction in C1 requesting two classes. Only classes that had good alignments and contained full channel particles were included in subsequent rounds of classification. 40,896 particles from the best class were then subjected to ab initio reconstruction in C1 requesting three classes, which gave a class with only side, a class with only top/bottom, and a good class with 23,378 particles. These 23,378 particles were used for a final ab initio reconstruction using three classes, and gave 21,663 particles that sorted into a class with a straight transmembrane region (14,992 particles) and a class where the transmembrane region was more bent with the Kir6.2 core puckered up towards the extracellular space (6,657 particles). Further rounds of ab initio reconstruction resulted in equivalent classes without further improvement in particle classification. The particles were re-extracted using a 600 pixel box at 0.8265 Å/pix, duplicate particles within 20 Å from each other on the micrograph were removed, then used as input for non-uniform refinement⁶¹ in C1 with the 6,657 particle map reconstruction at 6.4 Å resolution and the 14,115 particle map reconstruction at 3.4 Å resolution. A non-uniform refinement in C4 symmetry imposed with the 14,115 particles resulted in a 2.9 Å resolution reconstructed cryoEM map using cryoSPARC auto mask tightening (Supplementary Fig. 1). The auto-tightened FSC mask excluded the disordered NBD2 (Supplementary Fig. 1c). Masks for FSC calculation that included the full K_{ATP} channel with or without micelle were generated using molmap in UCSF ChimeraX version 1.2 (Chimera)⁶² (Supplementary Fig. 1c), and resampled on the full map grid (600³ pixels). The FSC calculated using these static masks yielded 3.3 Å resolution for the full channel without micelle (Supplementary Fig. 1b) and 3.5 Å resolution for the entire particle including the micelle ("Loose" in the FSC plot shown in Supplementary Fig. 1a, b).

To assess conformational heterogeneity for the entire dataset, duplicate and corrupt particles were removed from the set of 70,638 particles from 2D classification to give 66,049 particles and refined using cryoSPARC homogeneous refinement with C4 symmetry imposed (4.0 Å resolution), then 4-fold symmetry expanded to give 264,196 particles (Supplementary Fig. 2a). A mask covering the Kir6.2 tetramer, four TMD0 densities in SUR1, plus a large volume surrounding one of the SUR1 subunits to have a large region covering all

possible SUR1 locations, was generated using Chimera and used as a focused map to conduct 3D classification of symmetry expanded particles without particle alignment in cryoSPARC. This yielded two dominant classes: class 1 (106,781 particles), which resembles the open structure derived using the workflow shown in Supplementary Fig. 1a, and class 2 (53,201 particles), which has the Kir6.2^{Q252R} in the CTD-down position resembling previously published apo closed WT channel³⁸. Particles from each of these classes were further classified into four classes using cryoSPARC 3D classification, and the classes with the most divergent conformations were compared (Supplementary Fig. 2b-e). The reconstructed map from a C1 local refinement of 12,320 symmetry-expanded particles resembles the published apo closed WT structure (PDB ID 7UQR) and was well-fit by a rigid-body of that structure, but the resolution of the map (6.9 Å) was not sufficient to build a detailed atomic model.

To assess conformational heterogeneity within the high-resolution class of 14,115 particles of full-channel complexes that may have individual SUR1 subunits adopting independent conformations within a single K_{ATP} channel particle, particles were subjected to C4 symmetry expansion and 3D classification without particle alignment in cryoSPARC using the same mask described above. An initial focused 3D classification searching for 5 classes sorted particles into three dominant classes (class 0: 925 particles; class 1: 22474 particles; class 2: 10711 particles; class 3: 25664 particles; class 4: 194 particles). Class 1 to 3 showed three distinct SUR1 conformations, and subsequent local refinement using a loose mask covering the Kir6.2 tetramer, four TMD0 domains of SUR1, and one SUR1, resulted in map reconstructions of 3.12 Å, 3.99 Å, and 3.07 Å resolutions for class 1, 2, and 3, respectively (Supplementary Fig. 6a, b). In all three of these particle classes, the NBDs are separated, but with substantial differences between the relative positions of NBD2, and all have better resolved maps corresponding to the NBD2 than for the overall consensus C4 non-uniform refinement.

In the C4 reconstruction of the full K_{ATP} channel particle, there is good density for nearly every side chain of Kir6.2 except for the N-terminal 31 residues and the C-terminal tail beyond residue 352. TMD0 and the transmembrane helices of SUR1 also have clear density, with unclear density for the dynamic NBDs and loop regions, especially NBD2 which is poorly resolved due to apparent high flexibility when in the open conformation without NBD dimerization conditions.

To create an initial structural model, PDB ID 6BAA was fit into the reconstructed density for the full K_{ATP} channel particle using Chimera⁶³, and then refined in Phenix 1.20.1-4487 (Phenix)⁶⁴ as separate rigid bodies corresponding to TMD (32-171) and CTD 172-352 of Kir6.2 and TMD0/L0 (1-284), TMD1 (285-614), NBD1 (615-928), NBD1-TMD2-linker (992-999), TMD2 (1000-1319) and NBD2 (1320-1582). All sidechains and missing loops that had clear density were then built manually using Coot 0.9.8.1 (Coot)⁶⁵. The resulting model was further refined using Coot and Phenix iteratively until the statistics and fitting were satisfactory (Supplementary Table 1). Two models are presented. The first (PDB ID 8TI2) contains residues 32-352 for Kir6.2, and residues 1-1578 for SUR1 except for an extracellular loop (1043-1060), two loop regions (623-673 and 743-766) in NBD1 and the linker between NBD1 and TMD2 (928-986). Due to the resolution limitation of NBD2, all residues (except for proline) of NBD2 in this model are stubbed at C β . The second model (PDB ID 8TI1) has the highly flexible NBD2 removed⁶⁶. The N-terminal peptide of Kir6.2, which in closed NBD-separated structures rests between TMD1 and TMD2 of SUR1^{38,41}, is not observed in this conformation.

In addition to protein density, N-acetylglucosamine (NAG), which is the common core of N-linked glycosylation, is modeled in the distinctively large density at the side chain of N10 in each SUR1 (Fig. 1b). In addition, densities corresponding to two amphipathic molecules were observed at the interface between Kir6.2 and SUR1 and were modeled as two C18:0/20:4 PI(4,5)P₂ molecules, which gave the best fit

compared to other endogenous phospholipids and the detergent used to solubilize the membrane (see Supplementary Fig. 3a–e). Three other lipid densities per SUR1 monomer were also observed and modeled as phosphatidylserine or phosphatidylethanolamine (Supplementary Fig. 3f, g). The resulting model was further refined using Coot⁶⁵ and Phenix^{64,67,68} iteratively until the statistics and fitting were satisfactory (Supplementary Table 1). All structure figures were produced with Chimera⁶³, ChimeraX⁶², and PyMol (<http://www.pymol.org>). Pore radius calculations were performed with HOLE implemented in Coot⁶⁵.

Electrophysiology

For electrophysiology experiments, COSm6 cells were co-transfected with various combination of WT or mutant SUR1 and Kir6.2 cDNAs (SUR1 in pECE and Kir6.2 in pCDNA3) along with the cDNA for the Green Fluorescent Protein (to facilitate identification of transfected cells) using FuGENE[®] 6 (Promega). Mutant SUR1 and Kir6.2 were constructed using QuikChange (mutagenesis primers are shown in Supplementary Table 2). Cells were plated onto glass coverslips 24 h after transfection and recordings made in the following two days. All experiments were performed at room temperature⁶⁹. Micropipettes were pulled from non-heparinized Kimble glass (Fisher Scientific) on a horizontal puller (Sutter Instrument). Electrode resistance was typically 1–2 M Ω when filled with K-INT solution containing 140 mM KCl, 10 mM K-HEPES, 1 mM K-EGTA, 1 mM EDTA, pH 7.3. ATP was added as the potassium salt. Inside-out patches of cells bathed in K-INT were voltage-clamped with an Axopatch 1D amplifier (Axon Instruments). ATP or porcine brain PIP₂ (Avanti Polar Lipids; prepared in K-INT and bath sonicated in ice water for 30 min before use) were added to K-INT as specified in the figure legend. All currents were measured at a membrane potential of –50 mV (pipette voltage = +50 mV). Data were analyzed using pCLAMP10 software (Axon Instrument). Off-line analysis was performed using Clampfit and GraphPad. Data were presented as mean \pm standard error of the mean (S.E.M). ATP inhibition dose-response curves were obtained by fitting data to the Hill equation ($I_{rel} = 1/(1 + ([ATP]/IC_{50})^H)$), where I_{rel} is the current relative to the maximum currents in K-INT solution (expressed as % current in Fig. 7c and Supplementary Fig. 7a), IC_{50} is the ATP concentration that causes half-maximal inhibition, and H is the Hill coefficient. Note H was allowed to vary for the curves shown in Fig. 7c and Supplementary Fig. 7a.

Rb⁺ efflux assay

COSm6 cells were transiently transfected with various combinations of WT or mutant SUR1 and Kir6.2 cDNAs using FuGENE[®] 6. Untransfected cells were included as background control. Cells were cultured in medium containing 5 mM RbCl overnight. The next day, cells were washed quickly twice in Ringer's solution (5.4 mM KCl, 150 mM NaCl, 1 mM MgCl₂, 0.8 mM NaH₂PO₄, 2 mM CaCl₂, 25 mM HEPES, pH 7.2) with no RbCl. Rb⁺ efflux was measured by incubating cells in Ringer's solution (for experiments shown in Fig. 7d) or Ringer's solution supplemented with 5 mM glucose (for experiments shown in Supplementary Fig. 7b) over a 40 min period. Inclusion of 5 mM glucose increases intracellular ATP/ADP ratios to suppress channel activity, allowing for better detection of channels with mild gain-of-function phenotype as shown in some of the mutant channels in Supplementary Fig. 7b. At the end of the 40 min incubation, Efflux solution was collected and cells were lysed in Ringer's solution plus 1% Triton X-100. Rb⁺ concentrations in both the efflux solution and cell lysate were measured using an Atomic Adsorption Instrument Ion Channel Reader (ICR) 8100 from Aurora Biomed. Percent efflux was calculated by dividing Rb⁺ in the efflux solution over total Rb⁺ in the efflux solution and cell lysate. For each experiment, duplicates were included as technical repeats and the average was taken as the experimental value. For all channel combinations, separate transfections were carried out in parallel as biological repeats, as specified in the figure legends. Data were presented as mean \pm standard error of the mean (S.E.M) and

statistical analysis was performed by one-way ANOVA with Tukey's post hoc test in GraphPad.

Reporting summary

Further information on research design is available in the Nature Portfolio Reporting Summary linked to this article.

Data availability

The data that support this study are available from the corresponding authors upon request. The cryo-EM maps have been deposited in the Electron Microscopy Data Bank (EMDB) as [EMD-41278](#) (NBD2 modeled as main chain atoms only), [EMD-41277](#) (NBD2 not modeled), and [EMD-43766](#) (apo closed SUR1/Kir6.2Q52R). Structural models have been deposited in the Protein Data Bank (PDB) under accession code [8TI2](#) (NBD2 modeled as main chain atoms only), and [8TI1](#) (NBD2 not modeled). Previously published structures referred to in this article include: [7UQR](#) and [EMD-26320](#); [7TYS](#) and [EMD-26193](#); [6BAA](#) and [EMD-7073](#); [7W4O](#) and [EMD-32310](#); [7SSX](#) and [EMD-24842](#). The source data underlying Figs. 3b–d, 7c and d, and Supplementary Fig. 7 are provided as a Source Data file. Source data are provided with this paper.

References

1. Aguilar-Bryan, L. & Bryan, J. Molecular biology of adenosine triphosphate-sensitive potassium channels. *Endocr. Rev.* **20**, 101–135 (1999).
2. Ashcroft, F. M. K(ATP) channels and insulin secretion: a key role in health and disease. *Biochem Soc. Trans.* **34**, 243–246, (2006).
3. Nichols, C. G. K_{ATP} channels as molecular sensors of cellular metabolism. *Nature* **440**, 470–476 (2006).
4. Clement, J. P. T. et al. Association and stoichiometry of K(ATP) channel subunits. *Neuron* **18**, 827–838 (1997).
5. Shyng, S. & Nichols, C. G. Octameric stoichiometry of the K_{ATP} channel complex. *J. Gen. Physiol.* **110**, 655–664 (1997).
6. Driggers, C. M. & Shyng, S. L. Mechanistic insights on K_{ATP} channel regulation from cryo-EM structures. *J. Gen. Physiol.* **155**, e202113046 (2023).
7. Puljung, M. C. Cryo-electron microscopy structures and progress toward a dynamic understanding of K_{ATP} channels. *J. Gen. Physiol.* **150**, 653–669 (2018).
8. ElSheikh, A. & Shyng, S. L. K(ATP) channel mutations in congenital hyperinsulinism: progress and challenges towards mechanism-based therapies. *Front. Endocrinol. (Lausanne)* **14**, 1161117 (2023).
9. Rosenfeld, E., Ganguly, A. & De Leon, D. D. Congenital hyperinsulinism disorders: genetic and clinical characteristics. *Am. J. Med. Genet. C: Semin Med. Genet.* **181**, 682–692 (2019).
10. Pipatpolkai, T., Usher, S., Stansfeld, P. J. & Ashcroft, F. M. New insights into K_{ATP} channel gene mutations and neonatal diabetes mellitus. *Nat. Rev. Endocrinol.* **16**, 378–393 (2020).
11. Baukowitz, T. et al. PIP₂ and PIP as determinants for ATP inhibition of K_{ATP} channels. *Science* **282**, 1141–1144 (1998).
12. Shyng, S. L. & Nichols, C. G. Membrane phospholipid control of nucleotide sensitivity of K_{ATP} channels. *Science* **282**, 1138–1141 (1998).
13. Hibino, H. et al. Inwardly rectifying potassium channels: their structure, function, and physiological roles. *Physiol. Rev.* **90**, 291–366 (2010).
14. Dickson, E. J. & Hille, B. Understanding phosphoinositides: rare, dynamic, and essential membrane phospholipids. *Biochem. J.* **476**, 1–23 (2019).
15. Barneda, D., Cosulich, S., Stephens, L. & Hawkins, P. How is the acyl chain composition of phosphoinositides created and does it matter? *Biochem. Soc. Trans.* **47**, 1291–1305 (2019).
16. Enkvetchakul, D., Loussouarn, G., Makhina, E., Shyng, S. L. & Nichols, C. G. The kinetic and physical basis of K(ATP) channel

- gating: toward a unified molecular understanding. *Biophys. J.* **78**, 2334–2348 (2000).
17. Hansen, S. B., Tao, X. & MacKinnon, R. Structural basis of PIP2 activation of the classical inward rectifier K⁺ channel Kir2.2. *Nature* **477**, 495–498 (2011).
 18. Niu, Y., Tao, X., Touhara, K. K. & MacKinnon, R. Cryo-EM analysis of PIP2 regulation in mammalian GIRK channels. *Elife* **9**, e60552 (2020).
 19. Whorton, M. R. & MacKinnon, R. Crystal structure of the mammalian GIRK2 K⁺ channel and gating regulation by G proteins, PIP2, and sodium. *Cell* **147**, 199–208 (2011).
 20. Zhang, Y., Tao, X. & MacKinnon, R. Correlation between structure and function in phosphatidylinositol lipid-dependent Kir2.2 gating. *Proc. Natl Acad. Sci. USA* **119**, e2114046119 (2022).
 21. Tucker, S. J., Gribble, F. M., Zhao, C., Trapp, S. & Ashcroft, F. M. Truncation of Kir6.2 produces ATP-sensitive K⁺ channels in the absence of the sulphonylurea receptor. *Nature* **387**, 179–183 (1997).
 22. Li, N. et al. Structure of a pancreatic ATP-sensitive potassium channel. *Cell* **168**, 101–110.e10 (2017).
 23. Martin, G. M. et al. Cryo-EM structure of the ATP-sensitive potassium channel illuminates mechanisms of assembly and gating. *Elife* **6**, e24149 (2017).
 24. Lee, K. P. K., Chen, J. & MacKinnon, R. Molecular structure of human K_{ATP} in complex with ATP and ADP. *Elife* **6**, e32481 (2017).
 25. Babenko, A. P. & Bryan, J. SUR domains that associate with and gate K_{ATP} pores define a novel gatekeeper. *J. Biol. Chem.* **278**, 41577–41580 (2003).
 26. Chan, K. W., Zhang, H. & Logothetis, D. E. N-terminal transmembrane domain of the SUR controls trafficking and gating of Kir6 channel subunits. *EMBO J.* **22**, 3833–3843 (2003).
 27. Martin, G. M., Patton, B. L. & Shyng, S. L. K(ATP) channels in focus: Progress toward a structural understanding of ligand regulation. *Curr. Opin. Struct. Biol.* **79**, 102541 (2023).
 28. Zhao, C. & MacKinnon, R. Molecular structure of an open human K_{ATP} channel. *Proc. Natl Acad. Sci. USA* **118**, e2112267118 (2021).
 29. Wang, M., Wu, J. X., Ding, D. & Chen, L. Structural insights into the mechanism of pancreatic K_{ATP} channel regulation by nucleotides. *Nat. Commun.* **13**, 2770 (2022).
 30. Wang, M., Wu, J. X., Ding, D. & Chen, L. Structural insights into the mechanism of pancreatic K(ATP) channel regulation by nucleotides. *Nat. Commun.* **13**, 2770 (2022).
 31. Lin, C. W., Yan, F., Shimamura, S., Barg, S. & Shyng, S. L. Membrane phosphoinositides control insulin secretion through their effects on ATP-sensitive K⁺ channel activity. *Diabetes* **54**, 2852–2858 (2005).
 32. Shyng, S. L. et al. Modulation of nucleotide sensitivity of ATP-sensitive potassium channels by phosphatidylinositol-4-phosphate 5-kinase. *Proc. Natl Acad. Sci. USA* **97**, 937–941 (2000).
 33. Rohacs, T. et al. Specificity of activation by phosphoinositides determines lipid regulation of Kir channels. *Proc. Natl Acad. Sci. USA* **100**, 745–750 (2003).
 34. Koster, J. C., Remedi, M. S., Dao, C. & Nichols, C. G. ATP and sulphonylurea sensitivity of mutant ATP-sensitive K⁺ channels in neonatal diabetes: implications for pharmacogenomic therapy. *Diabetes* **54**, 2645–2654 (2005).
 35. Proks, P. et al. Molecular basis of Kir6.2 mutations associated with neonatal diabetes or neonatal diabetes plus neurological features. *Proc. Natl Acad. Sci. USA* **101**, 17539–17544 (2004).
 36. Tammaro, P., Girard, C., Molnes, J., Njolstad, P. R. & Ashcroft, F. M. Kir6.2 mutations causing neonatal diabetes provide new insights into Kir6.2-SUR1 interactions. *EMBO J.* **24**, 2318–2330 (2005).
 37. Suh, B. C. & Hille, B. PIP2 is a necessary cofactor for ion channel function: how and why? *Annu Rev. Biophys.* **37**, 175–195 (2008).
 38. Sung, M. W. et al. Ligand-mediated structural dynamics of a mammalian pancreatic K_{ATP} channel. *J. Mol. Biol.* **434**, 167789 (2022).
 39. Xu, H. et al. Distinct histidine residues control the acid-induced activation and inhibition of the cloned K(ATP) channel. *J. Biol. Chem.* **276**, 38690–38696 (2001).
 40. Martin, G. M., Kandasamy, B., DiMaio, F., Yoshioka, C. & Shyng, S. L. Anti-diabetic drug binding site in a mammalian K_{ATP} channel revealed by Cryo-EM. *Elife* **6**, e31054 (2017).
 41. Martin, G. M. et al. Mechanism of pharmacochaperoning in a mammalian K_{ATP} channel revealed by cryo-EM. *Elife* **8**, e46417 (2019).
 42. Ding, D., Wang, M., Wu, J. X., Kang, Y. & Chen, L. The structural basis for the binding of repaglinide to the pancreatic K_{ATP} channel. *Cell Rep.* **27**, 1848–1857.e1844 (2019).
 43. Krissinel, E. & Henrick, K. Inference of macromolecular assemblies from crystalline state. *J. Mol. Biol.* **372**, 774–797 (2007).
 44. Ribalet, B., John, S. A. & Weiss, J. N. Regulation of cloned ATP-sensitive K channels by phosphorylation, MgADP, and phosphatidylinositol biphosphate (PIP(2)): a study of channel rundown and reactivation. *J. Gen. Physiol.* **116**, 391–410 (2000).
 45. Pratt, E. B., Zhou, Q., Gay, J. W. & Shyng, S. L. Engineered interaction between SUR1 and Kir6.2 that enhances ATP sensitivity in K_{ATP} channels. *J. Gen. Physiol.* **140**, 175–187 (2012).
 46. Tammaro, P., Proks, P. & Ashcroft, F. M. Functional effects of naturally occurring KCNJ11 mutations causing neonatal diabetes on cloned cardiac K_{ATP} channels. *J. Physiol.* **571**, 3–14 (2006).
 47. Wu, J. X. et al. Ligand binding and conformational changes of SUR1 subunit in pancreatic ATP-sensitive potassium channels. *Protein Cell* **9**, 553–567 (2018).
 48. Pratt, E. B., Tewson, P., Bruederle, C. E., Skach, W. R. & Shyng, S. L. N-terminal transmembrane domain of SUR1 controls gating of Kir6.2 by modulating channel sensitivity to PIP2. *J. Gen. Physiol.* **137**, 299–314 (2011).
 49. Mandala, V. S. & MacKinnon, R. The membrane electric field regulates the PIP(2)-binding site to gate the KCNQ1 channel. *Proc. Natl Acad. Sci. USA* **120**, e2301985120 (2023).
 50. Wang, W., Whorton, M. R. & MacKinnon, R. Quantitative analysis of mammalian GIRK2 channel regulation by G proteins, the signaling lipid PIP2 and Na⁺ in a reconstituted system. *Elife* **3**, e03671 (2014).
 51. Pipatpolkai, T., Usher, S. G., Vedovato, N., Ashcroft, F. M. & Stansfeld, P. J. The dynamic interplay of PIP(2) and ATP in the regulation of the K(ATP) channel. *J. Physiol.* **600**, 4503–4519 (2022).
 52. Cukras, C. A., Jeliaskova, I. & Nichols, C. G. The role of NH2-terminal positive charges in the activity of inward rectifier K_{ATP} channels. *J. Gen. Physiol.* **120**, 437–446 (2002).
 53. Usher, S. G., Ashcroft, F. M. & Puljung, M. C. Nucleotide inhibition of the pancreatic ATP-sensitive K⁺ channel explored with patch-clamp fluorometry. *Elife* **9**, e52775 (2020).
 54. Salonen, L. M., Ellermann, M. & Diederich, F. Aromatic rings in chemical and biological recognition: energetics and structures. *Angew. Chem. Int. Ed. Engl.* **50**, 4808–4842 (2011).
 55. Ma, J. C. & Dougherty, D. A. The Cation-minus signpi Interaction. *Chem. Rev.* **97**, 1303–1324 (1997).
 56. De Franco, E. et al. Update of variants identified in the pancreatic beta-cell K(ATP) channel genes KCNJ11 and ABCC8 in individuals with congenital hyperinsulinism and diabetes. *Hum. Mutat.* **41**, 884–905 (2020).
 57. Himmel, B. & Nagel, G. Protein kinase-independent activation of CFTR by phosphatidylinositol phosphates. *EMBO Rep.* **5**, 85–90 (2004).
 58. Sung, M. W. et al. Vascular K_{ATP} channel structural dynamics reveal regulatory mechanism by Mg-nucleotides. *Proc. Natl Acad. Sci. USA* **118**, e2109441118 (2021).
 59. Driggers, C. M. & Shyng, S. L. Production and purification of ATP-sensitive potassium channel particles for cryo-electron microscopy. *Methods Enzymol.* **653**, 121–150 (2021).

60. Punjani, A., Rubinstein, J. L., Fleet, D. J. & Brubaker, M. A. cryoSPARC: algorithms for rapid unsupervised cryo-EM structure determination. *Nat. Methods* **14**, 290–296 (2017).
61. Punjani, A., Zhang, H. & Fleet, D. J. Non-uniform refinement: adaptive regularization improves single-particle cryo-EM reconstruction. *Nat. Methods* **17**, 1214–1221 (2020).
62. Pettersen, E. F. et al. UCSF ChimeraX: Structure visualization for researchers, educators, and developers. *Protein Sci.* **30**, 70–82 (2021).
63. Pettersen, E. F. et al. UCSF Chimera-a visualization system for exploratory research and analysis. *J. Comput. Chem.* **25**, 1605–1612 (2004).
64. Afonine, P. V. et al. Real-space refinement in PHENIX for cryo-EM and crystallography. *Acta Crystallogr D: Struct. Biol.* **74**, 531–544 (2018).
65. Emsley, P., Lohkamp, B., Scott, W. G. & Cowtan, K. Features and development of Coot. *Acta Crystallogr D: Biol. Crystallogr* **66**, 486–501 (2010).
66. Dawaliby, R. et al. Phosphatidylethanolamine is a key regulator of membrane fluidity in eukaryotic cells. *J. Biol. Chem.* **291**, 3658–3667 (2016).
67. Echols, N. et al. Graphical tools for macromolecular crystallography in PHENIX. *J. Appl. Crystallogr.* **45**, 581–586 (2012).
68. Liebschner, D. et al. Macromolecular structure determination using X-rays, neutrons and electrons: recent developments in Phenix. *Acta Crystallogr. D: Struct. Biol.* **75**, 861–877 (2019).
69. Devaraneni, P. K., Martin, G. M., Olson, E. M., Zhou, Q. & Shyng, S. L. Structurally distinct ligands rescue biogenesis defects of the K_{ATP} channel complex via a converging mechanism. *J. Biol. Chem.* **290**, 7980–7991 (2015).

Acknowledgements

A portion of this research was supported by NIH grant U24GM129547 and performed at the Pacific Northwest Cryo-EM Center (PNCC) at Oregon Health & Science University and accessed through EMSL (grid.436923.9), a DOE Office of Science User Facility sponsored by the Office of Biological and Environmental Research, with special thanks to Dr. Nancy Meyer for help with cryoEM data collection. We acknowledge support from the National Institutes of Health grant R01DK066485 (to S.L.S.) and R01GM145784-02S1 (to S.L.S.), the OHSU Tartar trust fellowship (to C.M.D.), the Taiwan Ministry of Science and Technology Graduate Students Study Abroad Program scholarship 111-2917-I-006-004 (to Y.Y.K.), and the Egyptian government predoctoral scholarship GM 1109 (to A.E.). We are grateful to Zhongying Yang for help preparing adenovirus constructs and John Allen for preparing plasmids. We thank Drs. Katarzyna Walczewska, Min Woo Sung, and Bruce L. Patton for helpful discussions and Dr. Bruce L. Patton for comments on the manuscript.

Author contributions

C.M.D. designed and performed cryoEM experiments, analyzed data, prepared figures, wrote and edited the manuscript. Y.Y.K. performed electrophysiology and Rb⁺ efflux experiments, analyzed data, prepared figures, and edited the manuscript. P.Z. analyzed cryoEM data, prepared Supplementary Fig. 1b and edited the manuscript. A.E. performed Rb⁺ efflux experiments, prepared figures and edited the manuscript. S.L.S. conceived the project, performed electrophysiology experiments, prepared figures, wrote and edited the manuscript.

Competing interests

The authors declare no competing interests.

Additional information

Supplementary information The online version contains supplementary material available at <https://doi.org/10.1038/s41467-024-46751-5>.

Correspondence and requests for materials should be addressed to Camden M. Driggers or Show-Ling Shyng.

Peer review information *Nature Communications* thanks the anonymous reviewers for their contribution to the peer review of this work. A peer review file is available.

Reprints and permissions information is available at <http://www.nature.com/reprints>

Publisher's note Springer Nature remains neutral with regard to jurisdictional claims in published maps and institutional affiliations.

Open Access This article is licensed under a Creative Commons Attribution 4.0 International License, which permits use, sharing, adaptation, distribution and reproduction in any medium or format, as long as you give appropriate credit to the original author(s) and the source, provide a link to the Creative Commons licence, and indicate if changes were made. The images or other third party material in this article are included in the article's Creative Commons licence, unless indicated otherwise in a credit line to the material. If material is not included in the article's Creative Commons licence and your intended use is not permitted by statutory regulation or exceeds the permitted use, you will need to obtain permission directly from the copyright holder. To view a copy of this licence, visit <http://creativecommons.org/licenses/by/4.0/>.

© The Author(s) 2024